Stability analysis of the spatiotemporal Lugiato-Lefever model for Kerr optical frequency combs in the anomalous and normal dispersion regimes

Cyril Godey,[1] Irina V. Balakireva,[2] Aurélien Coillet,[2] and Yanne K. Chembo[2,*]

[1] *University of Franche-Comté, Department of Mathematics [CNRS UMR6623], 16 Route de Gray, 25030 Besançon cedex, France*

[2] *FEMTO-ST Institute [CNRS UMR6174], Optics Department, 16 Route de Gray, 25030 Besançon cedex, France*

(Received 11 August 2013; revised manuscript received 23 April 2014; published 16 June 2014)

We propose a detailed stability analysis of the Lugiato-Lefever model for Kerr optical frequency combs in whispering-gallery-mode resonators when they are pumped in either the anomalous- or normal-dispersion regime. We analyze the spatial bifurcation structure of the stationary states depending on two parameters that are experimentally tunable; namely, the pump power and the cavity detuning. Our study demonstrates that, in both the anomalous- and normal-dispersion cases, nontrivial equilibria play an important role in this bifurcation map because their associated eigenvalues undergo critical bifurcations that are actually foreshadowing the existence of localized and extended spatial dissipative structures. The corresponding bifurcation maps are evidence of a considerable richness from a dynamical standpoint. The case of anomalous dispersion is indeed the most interesting from the theoretical point of view because of the considerable variety of dynamical behavior that can be observed. For this case we study the emergence of super- and subcritical Turing patterns (or primary combs) in the system via modulational instability. We determine the areas where bright isolated cavity solitons emerge, and we show that soliton molecules can emerge as well. Very complex temporal patterns can actually be observed in the system, where solitons (or soliton complexes) coexist with or without mutual interactions. Our investigations also unveil the mechanism leading to the phenomenon of breathing solitons. Two routes to chaos in the system are identified; namely, a route via the destabilization of a primary comb, and another via the destabilization of solitons. For the case of normal dispersion, we unveil the mechanism leading to the emergence of weakly stable Turing patterns. We demonstrate that this weak stability is justified by the distribution of stable and unstable fixed points in the parameter space (flat states). We show that dark cavity solitons can emerge in the system, and also show how these solitons can coexist in the resonator as long as they do not interact with each other. We find evidence of breather solitons in this normal dispersion regime as well. The Kerr frequency combs corresponding to all these spatial dissipative structures are analyzed in detail, along with their stability properties. A discussion is led about the possibility to gain unifying comprehension of the observed spectra from the dynamical complexity of the system.

DOI: 10.1103/PhysRevA.89.063814 PACS number(s): 42.65.Sf, 42.62.Eh, 42.65.Hw, 42.65.Tg

I. INTRODUCTION

A Kerr comb is a set of equidistant spectral components generated through the optical pumping of an ultrahigh-quality-factor whispering-gallery-mode (WGM) resonator with Kerr nonlinearity. In this system, the WGM resonator is pumped by a continuous-wave (cw) laser, and the pump photons are transferred through four-wave mixing (FWM) to neighboring cavity eigenmodes. All these excited modes are coupled through FWM and, as a result, may excite an even greater number of modes. This process can generate as much as several hundred oscillating modes, which are the spectral components constituting the so-called Kerr comb.

Kerr-comb generators are characterized by their conceptual simplicity, structural robustness, small size, and low power consumption. They are therefore promising candidates to replace femtosecond mode-locked lasers in applications where these features are of particular relevance. The theoretical understanding of Kerr-comb generation in whispering-gallery-mode resonators is currently the focus of a worldwide activity that is motivated by the wide range of potential applications [1–8]. Another incentive is the necessity to understand the complex light-matter interactions that are induced by the strong confinement of long-lifetime photons in nonlinear media.

Early models for Kerr-comb generation were based on a modal-expansion approach [9–11], which used a large set of coupled nonlinear ordinary differential equations to track the individual dynamics of the WGMs. This formalism enabled researchers to determine threshold phenomena and to explain the role of dispersion as well as some of the mechanisms leading to Kerr-comb generation. However, this modal model becomes difficult to analyze theoretically when the number of excited modes is higher than five [11].

An alternative paradigm has been introduced recently and is based on the fact that, in the system under study, light circumferentially propagates inside the resonator and can be treated as if it were propagating along an unfolded trajectory with periodic boundary conditions [12–15]. In this case, the system can be modeled by a spatiotemporal formalism known as the Lugiato-Lefever equation (LLE), which is a nonlinear Schrödinger equation (NLSE) with damping, detuning, and driving [16]. The variable of the LLE is the overall intracavity field, which is the sum of the modal fields described by the modal model. Equivalence between the modal approach and the spatiotemporal formalism has been demonstrated recently and enables us to understand the Kerr-comb generation process from different viewpoints: the modal approach is useful to investigate threshold phenomena when only few modes are

*yanne.chembo@femto-st.fr

 ©2014 American Physical Society

involved, while the spatiotemporal formalism is suitable when a very large number of interacting modes are involved [11]. In this latter case, mode-locking between the modes can lead to the formation of narrow pulses, such as cavity solitons, for example. From a more general perspective, the LLE formalism shows that Kerr combs are the spectral signature of dissipative patterns or localized structures in WGM resonators [17].

Among the various parameters that are relevant to understand Kerr-comb generation, group velocity dispersion (GVD) is one of the most important. GVD in WGM resonators can be either normal or anomalous, and the real-valued parameter corresponding to GVD has opposite signs depending on the dispersion regime. From a mathematical point of view, the solutions to be expected when using the constitutive dynamical equations are therefore different; from the physics standpoint, the phenomenology is intrinsically different as well. However, the role of dispersion in Kerr-comb formation is still a wide-open problem, and the various solutions that are expected to arise depending on the sign of dispersion are to a large extent unknown.

Almost all previous research has been devoted to the investigation of Kerr-comb generation in the anomalous group velocity dispersion (GVD) regime. In fact, it was thought for a long time that normal-GVD Kerr-comb generation was impossible but, later on, it was shown to occur only under fairly exceptional circumstances (see, for example, Refs. [17–19]). This explains why the quasitotality of the scientific literature on Kerr combs assumes a laser-pump frequency in the anomalous-GVD regime for the bulk material of the resonator.

When the dispersion is anomalous, earlier studies on Kerr-comb generation have shown that, above a given threshold, the long-lifetime photons originating from the pump interact nonlinearly with the medium and populate the neighboring cavity modes through four-wave mixing (FWM). The resulting permanent state features an all-to-all coupling among the excited modes, which can enable various dynamical outputs such as phase-locked (through Turing patterns or solitons), pulsating, and even chaotic states. In particular, the phase-locked states are expected to be useful for a wide spectrum of applications [1–8].

Comprehensive studies where all these behaviors are associated with well-identified regions of the parameter space are scarce. Most research articles so far have focused on specific phenomenologies (modulational instability, solitons, chaos, breathers, etc.) and our objective in this paper is to provide a larger viewpoint for understanding of Kerr-comb generation with either anomalous or normal GVD. More specifically, we perform a stability analysis of the various solutions that can arise when a nonlinear WGM resonator is pumped. The control parameters of the two-dimensional stability map are those that are the most easily accessible at the experimental level; that is, the pump power and the laser detuning relative to the cavity resonance.

The plan of this article is the following: In the next section, we present the model that is used to perform the stability analysis. A short discussion will also be led to link the parameters of the model with the physical properties of the system under study. Section III is devoted to the equilibria of the system and their temporal stability, and we then investigate in Sec. IV the spatial bifurcations of the system. Section V focuses on the construction of bifurcation maps based on the eigenvalue distribution. Section VI is devoted to the analysis of the various solutions that can be obtained in the case of anomalous dispersion. Turing patterns (rolls) arising from modulational instability (MI) are shown to emerge in the system, and their super- or subcritical nature is analyzed in the time domain with respect to the detuning frequency of the pump laser. We also study the emergence of bright cavity solitons, soliton molecules, soliton breathers, and spatiotemporal chaos. Section VII focuses on solutions found in the case of normal dispersion. We analyze the emergence of weakly stable extended Turing patterns and also determine the basins of attraction of a wide variety of dark solitons and breathers. The main findings of this study are comprehensively reviewed in the last section, which concludes this article.

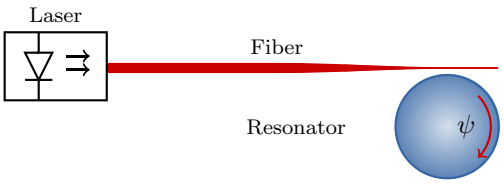

FIG. 1. (Color online) Schematic of a coupled WGM resonator. The pump radiation originates from a cw laser and the coupling is achieved by using, for example, a tapered fiber.

II. THE MODEL

The system under study is a WGM disk pumped by a cw pump laser radiation via evanescent coupling. The typical experimental setup is displayed in Fig. 1. The understanding of the various phenomena of interest requires a sound knowledge of the eigenmode structure of WGM cavities [20,21].

Let us consider a disk of main radius a and group velocity refraction index n_g at the laser pump frequency Ω_0. The simplest set of eigenmodes is the so-called fundamental family, which is characterized by a torus-like (or doughnut) spatial form inside the cavity. Each mode of this family can be unambiguously defined by a single eigennumber ℓ, which can be interpreted as the number of internal reflections that a photon undergoes in that mode in order to perform a round-trip along the rim of the disk.

Let us now consider that the pumped mode is ℓ_0. If we only consider the modes ℓ that are close to ℓ_0, their eigenfrequencies can be Taylor expanded as

$$\omega_\ell = \omega_{\ell_0} + \zeta_1(\ell - \ell_0) + \tfrac{1}{2}\zeta_2(\ell - \ell_0)^2, \qquad (1)$$

where $\zeta_1 = c/(an_g)$ is the intermodal angular frequency (or free spectral range, FSR), with c being the velocity of light in vacuum, while ζ_2 stands for the second-order dispersion which measures the nonequidistance of the eigenfrequencies at the lowest order (see Fig. 2). We have here restricted ourselves to the second order in the Taylor expansion, but nothing forbids us from considering higher-order dispersion terms if necessary. It is also interesting to note that the intracavity round-trip time is linked to the FSR by $T = 2\pi/\zeta_1$.

The eigenmodes that are sufficiently close to ℓ_0 are characterized by the same modal linewidth $\Delta\omega_{\text{tot}}$. More precisely,

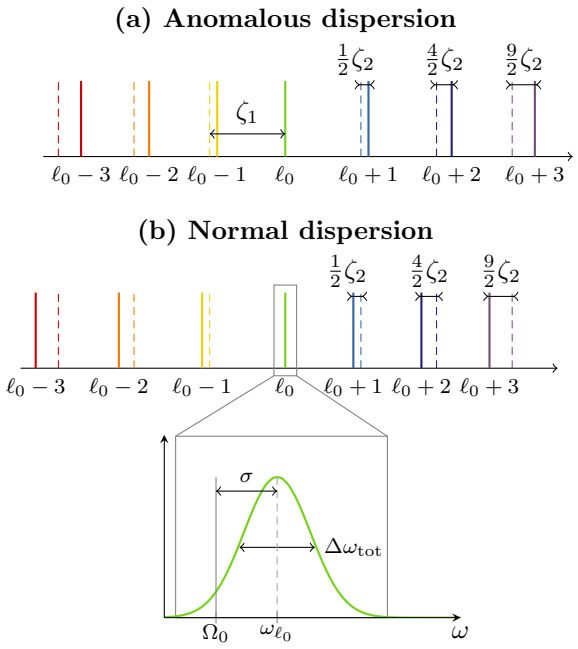

FIG. 2. (Color online) Eigenmodes of WGM resonator. The real location of the eigenfrequencies with anomalous or normal dispersion is represented by solid lines, while the dashed lines represent the location of the eigenfrequencies if the dispersion were null (perfect equidistance). The enlargement displays the relationship between the loaded linewidth $\Delta\omega_{\rm tot}$, the cold-resonance frequency ω_{ℓ_0}, the laser frequency Ω_0, and the cavity detuning $\sigma = \Omega_0 - \omega_{\ell_0}$. It is sometimes convenient to introduce the shifted eigennumber $l \equiv \ell - \ell_0$, so that the pumped mode is $l = 0$, while the side modes correspond to $l = \pm 1, \pm 2, \ldots$ [11]. In the case of anomalous dispersion, the eigenmodes are pulled rightward (blueshift), while in the case of normal dispersion, the eigenmodes are pulled leftward (redshift).

we have

$$\Delta\omega_{\rm tot} = \Delta\omega_{\rm in} + \Delta\omega_{\rm ext}, \tag{2}$$

where $\Delta\omega_{\rm in} = \omega_{\ell_0}/Q_{\rm in}$, $\Delta\omega_{\rm ext} = \omega_{\ell_0}/Q_{\rm ext}$, and $\Delta\omega_{\rm tot} = \omega_{\ell_0}/Q_{\rm tot}$ are respectively the intrinsic, extrinsic (or coupling), and total linewidths, while the quality factors Q are defined analogously. Interestingly, the modal linewidth $\Delta\omega_{\rm tot}$ can be viewed as a measure of the total losses of the resonator, since it is linked to the average photon lifetime $\tau_{\rm ph}$ as

$$\tau_{\rm ph} = \frac{1}{\Delta\omega_{\rm tot}}. \tag{3}$$

The normalized complex slowly varying envelopes $\mathcal{A}_\ell(t)$ of the various eigenmodes can be obtained by using the modal-expansion model proposed in Ref. [11]. The amplitudes were normalized such that $|\mathcal{A}_\ell|^2$ was the number of photons in the mode ℓ. The overall intracavity field $\mathcal{A}$ can be determined as a sum of the modal fields $\mathcal{A}_\ell$ and, in Ref. [14], a spatiotemporal Lugiato-Lefever formalism has been constructed in order to describe the dynamics of this total intracavity field. In its normalized form, this corresponding equation is the following partial differential equation:

$$\frac{\partial\psi}{\partial\tau} = -(1+i\alpha)\psi + i|\psi|^2\psi - i\frac{\beta}{2}\frac{\partial^2\psi}{\partial\theta^2} + F, \tag{4}$$

where $\psi(\theta,\tau)$ is the complex envelope of the total intracavity field, $\theta \in [-\pi,\pi]$ is the azimuthal angle along the circumference, and $\tau = t/(2\tau_{\rm ph})$ is the dimensionless time, with $\tau_{\rm ph}$ being the photon lifetime in the coupled cavity defined in Eq. (3). It is important to note that this equation has *periodic* boundary conditions, and that ψ represents the intracavity fields dynamics in the *moving frame*.

The other dimensionless parameters of this normalized LLE are the frequency detuning

$$\alpha = -\frac{2(\Omega_0 - \omega_{\ell_0})}{\Delta\omega_{\rm tot}} = -\frac{2\sigma}{\Delta\omega_{\rm tot}}, \tag{5}$$

where Ω_0 and ω_{ℓ_0} are, respectively, the angular frequencies of the pumping laser and the cold-cavity resonance, and the overall dispersion parameter

$$\beta = -\frac{2\zeta_2}{\Delta\omega_{\rm tot}}. \tag{6}$$

Note that the anomalous-GVD regime is defined by $\beta < 0$ while normal GVD corresponds to $\beta > 0$. Finally, by using the coupling formalism presented in Ref. [22] and used in Ref. [23] for optical resonators, the dimensionless external pump field intensity can be explicitly defined as

$$F = \sqrt{\frac{8g_0\Delta\omega_{\rm ext}}{\Delta\omega_{\rm tot}^3}\frac{P}{\hbar\Omega_0}}, \tag{7}$$

where P is the optical power (in W) of the laser pump at the input of the resonator. The nonlinear gain g_0 is equal to $n_2c\hbar\Omega_0^2/(n_0^2V_0)$, where n_0 and n_2 are, respectively, the linear and nonlinear refraction indices of the bulk material, and V_0 is the effective volume of the pumped mode. Note that since F is real valued and positive, the optical phase reference is arbitrarily set by this pump radiation for all practical purpose.

It is interesting to note that, as demonstrated in Ref. [14] which links the modal and spatiotemporal formalisms for Kerr-comb generation, the intracavity field can be expanded as

$$\psi(\theta,\tau) = \sum_l \Psi_l(\tau)e^{il\theta}, \tag{8}$$

with

$$\Psi_l(\tau) = \sqrt{\frac{2g_0}{\Delta\omega_{\rm tot}}}\mathcal{A}_\ell^*(\tau)e^{i\frac{1}{2}\beta l^2\tau}, \tag{9}$$

where $\mathcal{A}_\ell$ corresponds to the modal complex field envelopes introduced in Refs. [10,11], and $l \equiv \ell - \ell_0$ is the azimuthal eigennumber of the photons with respect to the pumped mode (which is therefore labeled $l = 0$, while the side modes correspond to $l = \pm 1, \pm 2, \ldots$). By inserting the expansion (8) into Eq. (4), it can be shown that the dynamics of the complex-valued slowly varying envelopes Ψ_l is ruled by

$$\frac{d\Psi_l}{d\tau} = \left[-(1+i\alpha) + i\frac{\beta}{2}l^2\right]\Psi_l + \delta(l)F + i\sum_{m,n,p}\delta(m-n+p-l)\Psi_m\Psi_n^*\Psi_p, \tag{10}$$

where $\delta(x)$ is the usual Kronecker function equal to 1 for $x = 0$ and to 0 otherwise, while m, n, p, and l are eigennumbers labeling the interacting modes following the

interaction $\hbar\omega_m + \hbar\omega_p \leftrightarrow \hbar\omega_n + \hbar\omega_l$. Note that the above modal model of Eq. (10) is strictly equivalent to the original modal-expansion formalism presented in Ref. [11]. However, Eq. (10) is significantly simpler and is much easier to simulate and to analyze than the former modal model for two reasons. The first reason is that the explicit time dependence is removed in the sum accounting for the four-wave mixing, and Eq. (10) is therefore totally autonomous: from a physical viewpoint, this is due to the fact that $\mathcal{A}_\ell$ was defined relative to the (nonequidistant) nominal eigenfrequencies ω_ℓ of the resonator (continuous lines in Fig. 2), while the modes Ψ_l are defined relative to the (equidistant) dispersion-shifted eigenfrequencies $\omega_\ell + \frac{1}{2}\zeta_2(\ell - \ell_0)^2$ (dashed lines in Fig. 2). The second reason is that the modal equations in Ψ_l are completely dimensionless, owing to the full normalization. It was shown in Ref. [14] that both the spatiotemporal and modal-expansion formalisms are equivalent. It has also been shown recently in Ref. [24] that the coupled-mode equations can be numerically simulated as fast as the LLE provided that the four-wave mixing terms are also computed by using the fast-Fourier transform.

It is useful to give some orders of magnitude in relation to the model of Eq. (4). Let us consider, for example, the case of mm-size ultrahigh-Q crystalline WGM resonators pumped around 1550 nm. The intermodal frequencies $\zeta_1/(2\pi)$ are of the order of 10 GHz, which corresponds to round-trip times of 100 ps and eigennumbers $\ell_0 \simeq \omega_{\ell_0}/\zeta_1 \sim 10^4$. On the other hand, the dispersion parameter $\zeta_2/2\pi$ is typically of the order of 10 kHz or less in absolute value. The intrinsic Q factors are typically of the order of 10^9, so that the corresponding photon lifetimes τ_{ph} are of the order of 1 μs, and the modal linewidths are of the order of 100 kHz. The pump power typically varies from 10 mW to 1 W. These parameters can be easily translated to those of the LLE: the frequency detuning α can be linearly scanned at the experimental level to any value, but relevant values typically range from -5 to 5 since off-resonance pumping occurs as soon as $|\alpha| > 1$. The absolute value of the dispersion parameter, $|\beta|$, is 10 to 1000 times smaller than unity. The pumping term F will typically range between 0 and 100. Accordingly, the normalized intracavity field will also have an order of magnitude $|\psi|^2 \sim 1$ around the threshold.

It is interesting to explain why the case $\beta = 0$ is not investigated in the present work. It had sometimes been considered that dispersion was necessarily detrimental to Kerr-comb generation, and that the zero-dispersion limit would be ideal to guarantee equidistance in the comb. The analysis of the modal-expansion model performed in Ref. [11] already showed that it is the opposite statement that is indeed correct: Kerr-comb generation is a priori possible for all but zero dispersion. The mathematical explanation of this statement is in fact strikingly simple from the standpoint of the spatiotemporal formalism of Eq. (4): setting β to zero would eliminate the spatial dependence of ψ, therefore allowing only for θ-independent solutions (flat states, characterized by a single frequency). The LLE would then degenerate into an autonomous set of two-dimensional ordinary differential equations describing the dynamics of the real and imaginary parts of ψ. It can be inferred from the Poincaré-Bendixon theorem that the only solutions might be stationary states and limit-cycles (temporally slowly varying flat states in this case, yielding a single frequency and modulation side modes located *within* the loaded resonance). It therefore appears that both Kerr nonlinearity and dispersion are necessary (but not sufficient) ingredients for Kerr-comb generation. Another important point is that, from a physical point of view, setting β to zero requires taking into account at least the first of all the higher-order dispersion terms (proportional to $\partial^n\psi/\partial\theta^n$ with $n \geqslant 3$) that is not null. Hence, in this regard, the case $\beta = 0$ would actually force us to consider a new problem that is more complex than the LLE from a physical point of view.

We will use the spatiotemporal Lugiato-Lefever formalism represented by Eq. (4) in order to investigate the various steady-state solutions that can emerge in the system when $\beta \neq 0$. The numerical simulations will be performed by using the split-step Fourier algorithm. It is noteworthy that this algorithm inherently assumes periodic boundary conditions because it is based on the fast Fourier transform (FFT). It is therefore a very fast and efficient simulation method in our case where the periodic conditions are indeed periodic [14]. Note that this FFT algorithm can be used to speed up the simulation of the modal-expansion model as well [24].

III. EQUILIBRIA AND THEIR TEMPORAL STABILITY

In this section, we aim to find the various equilibria of the system and determine their temporal stability.

All equilibria ψ_{e} are obtained from Eq. (4) by setting all the derivatives to zero, thereby yielding

$$F^2 = [1 + (\rho - \alpha)^2]\rho \equiv G(\alpha, \rho), \tag{11}$$

which is a cubic polynomial equation in $\rho = |\psi_{\mathrm{e}}|^2$. It is well known that this equation has one, two, or three real-valued solutions depending on the parameters α and F. Multiple solutions may arise in a polynomial equation when it has local extrema; in our case, this condition requires the existence of critical values of ρ such that the partial derivative

$$\frac{\partial G}{\partial \rho} = 3\rho^2 - 4\alpha\rho + \alpha^2 + 1 \tag{12}$$

is null. This condition yields a quadratic equation with a discriminant equal to $4(\alpha^2 - 3)$; therefore, if $|\alpha| < \sqrt{3}$, there are no such critical values for ρ whereas, for $|\alpha| \geqslant \sqrt{3}$, these critical values are

$$\rho_\pm(\alpha) = \frac{2\alpha \pm \sqrt{\alpha^2 - 3}}{3}, \tag{13}$$

and the corresponding pumping terms are

$$\begin{aligned} F^2_\pm(\alpha) &= G[\alpha, \rho_\mp(\alpha)] \\ &= \frac{2\alpha \mp \sqrt{\alpha^2 - 3}}{3}\left[1 + \left(\frac{\sqrt{\alpha^2 - 3} \pm \alpha}{3}\right)^2\right]. \end{aligned} \tag{14}$$

Hence, when $\alpha > \sqrt{3}$, there exists a range of pumping power $F^2 \in]F^2_-(\alpha), F^2_+(\alpha)[$ such that there are three equilibria ρ_1, ρ_2, and ρ_3 ordered as $\rho_1 \leqslant \rho_- \leqslant \rho_2 \leqslant \rho_+ \leqslant \rho_3$. On the one hand, it can be shown that, if these solutions are perturbed in the temporal domain, the extremal solutions ρ_1 and ρ_3 are always stable while the intermediate solution ρ_2 is always unstable.

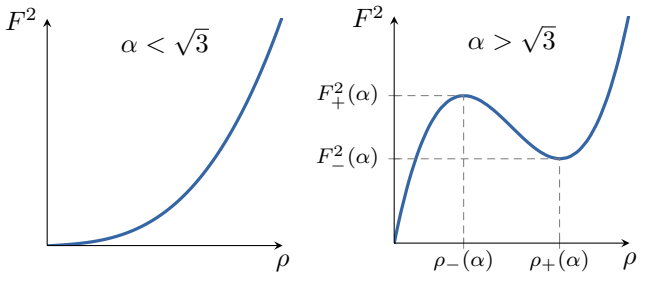

FIG. 3. (Color online) Relationship between the number of solutions and the pumping strength F. There is always only one solution for $\alpha < \sqrt{3}$, but for $\alpha > \sqrt{3}$, there is a range of pumping strengths F for which there are three solutions.

This is the well-known theory of hysteresis in dynamical systems with cubic nonlinearity. On the other hand, outside the interval $[F_-^2(\alpha), F_+^2(\alpha)]$, there is a unique equilibrium which is always stable. The same conclusion applies as well for every value of F^2 whenever $\alpha < \sqrt{3}$. The intermediate case where two solutions exist precisely corresponds to the boundary lines $F_-^2(\alpha)$ and $F_+^2(\alpha)$. Figure 3 shows how the multiple-equilibria states emerge as the value of the cavity detuning α increases. This analysis is actually equivalent to the one that was performed in Ref. [11] with the modal-expansion model, when the time dynamics was disregarded (temporal derivative set to zero).

IV. SPATIAL BIFURCATIONS

The objective of a spatial bifurcation study is to investigate the various stationary solutions of the system as a function of the parameters. The full study requires at least the calculation of the relevant normal forms around all the critical points and lines of the system. This task is indeed very complex, and can be circumvented by a simpler approach which can still provide insightful information about the spatial stability of the various solutions.

We start by setting the temporal derivative to zero and we rewrite the original Eq. (4) as

$$\frac{\partial^2 \psi_r}{\partial \theta^2} = \frac{2}{\beta}\left[\left(\psi_r^2 + \psi_i^2 - \alpha\right)\psi_r - \psi_i\right], \tag{15}$$

$$\frac{\partial^2 \psi_i}{\partial \theta^2} = \frac{2}{\beta}\left[\left(\psi_r^2 + \psi_i^2 - \alpha\right)\psi_i + \psi_r - F\right], \tag{16}$$

where $\psi = \psi_r + i\psi_i$, with ψ_r and ψ_i being, respectively, the real and complex parts of ψ. If we introduce the intermediate variable

$$\phi_{r,i} = \frac{\partial \psi_{r,i}}{\partial \theta}, \tag{17}$$

then Eq. (16) can be rewritten under the form of a four-dimensional flow:

$$\frac{\partial \psi_r}{\partial \theta} = \phi_r, \tag{18}$$

$$\frac{\partial \phi_r}{\partial \theta} = \frac{2}{\beta}\left(\psi_r^3 + \psi_i^2\psi_r - \alpha\psi_r - \psi_i\right), \tag{19}$$

$$\frac{\partial \psi_i}{\partial \theta} = \phi_i, \tag{20}$$

$$\frac{\partial \phi_i}{\partial \theta} = \frac{2}{\beta}\left(\psi_r^2\psi_i + \psi_i^3 - \alpha\psi_i + \psi_r - F\right). \tag{21}$$

The matrix of the linearized system around an equilibrium $\psi_e = \psi_{e,r} + i\psi_{e,i}$ is

$$\mathsf{J} = \begin{bmatrix} 0 & 1 & 0 & 0 \\ \frac{2}{\beta}\left(3\psi_{e,r}^2 + \psi_{e,i}^2 - \alpha\right) & 0 & \frac{2}{\beta}(2\psi_{e,r}\psi_{e,i} - 1) & 0 \\ 0 & 0 & 0 & 1 \\ \frac{2}{\beta}(2\psi_{e,r}\psi_{e,i} + 1) & 0 & \frac{2}{\beta}\left(\psi_{e,r}^2 + 3\psi_{e,i}^2 - \alpha\right) & 0 \end{bmatrix}, \tag{22}$$

and the eigenvalues λ of this Jacobian matrix obey the characteristic equation

$$\lambda^4 - \frac{4}{\beta}(2\rho - \alpha)\lambda^2 + \frac{4}{\beta^2}(3\rho^2 - 4\alpha\rho + \alpha^2 + 1) = 0. \tag{23}$$

As explained before, the sign of β is determined by the overall dispersion ($\beta < 0$ for anomalous GVD, and $\beta > 0$ for normal GVD).

Equation (23) is quadratic in λ^2; hence, we always have four eigenvalues which are either pairwise opposite (when real valued) or pairwise conjugated (when complex valued). It is also important to note that there is a quadruplet of eigenvalues *for each solution*. We will therefore have four eigenvalues in the area of the α-F^2 plane where there is a single equilibrium, twelve eigenvalues in the hysteresis area where there are three equilibria, and eight eigenvalues in the boundary lines where there are two solutions.

The nature (complex, real, or pure imaginary) of the eigenvalues is partially decided by the sign of the discriminant $\Delta = 16(\rho^2 - 1)/\beta^2$; that is, by the comparative value of the equilibrium ρ with regards to 1. We hereafter analyze in detail the nature of the eigenvalues as a function of the sign of this discriminant, which is decided by $\rho > 1$, $\rho = 1$, or $\rho < 1$. We will also see in Sec. V how the structural properties of these eigenvalues are controlled by the parameters α and F^2, thereby enabling us to plot an insightful bifurcation map.

A. First case: $\rho > 1$

In this case the paired solutions obey

$$\lambda^2 = \frac{2}{\beta}[2\rho - \alpha \pm \sqrt{\rho^2 - 1}]. \tag{24}$$

The product of these paired solutions is equal to $4(3\rho^2 - 4\alpha\rho + \alpha^2 + 1)/\beta^2$; that is, proportional to $\partial G/\partial\rho$ as defined in Eq. (12).

There are five subcases depending on the sign of this function and the sign of β:

(1) If $\partial G/\partial\rho > 0$, then

(i) If $\beta < 0$, the eigenvalues can be written as $(\lambda_{1,2}; \lambda_{3,4}) = (\pm a; \pm b)$ if $2\rho - \alpha < 0$ (this subcase is referred to as Type 1), and as $(\lambda_{1,2}; \lambda_{3,4}) = (\pm ia; \pm ib)$ if $2\rho - \alpha > 0$ (Type 3).

(ii) If $\beta > 0$, the eigenvalues are $(\lambda_{1,2}; \lambda_{3,4}) = (\pm a; \pm b)$ if $2\rho - \alpha > 0$ (Type 1), and as $(\lambda_{1,2}; \lambda_{3,4}) = (\pm ia; \pm ib)$ if $2\rho - \alpha < 0$ (Type 3).

(2) If $\partial G/\partial\rho = 0$, then

(i) If $\beta < 0$, the eigenvalues can be written as $(\lambda_{1,2};\lambda_{3,4}) = (\pm a;0)$ if $2\rho - \alpha < 0$ (Type 4), and as $(\lambda_{1,2};\lambda_{3,4}) = (0;\pm ib)$ if $2\rho - \alpha > 0$ (Type 5).

(ii) If $\beta > 0$, the eigenvalues are $(\lambda_{1,2};\lambda_{3,4}) = (\pm a;0)$ if $2\rho - \alpha > 0$ (Type 4) and $(\lambda_{1,2};\lambda_{3,4}) = (0;\pm ib)$ if $2\rho - \alpha < 0$ (Type 5).

(3) If $\partial G/\partial\rho < 0$, then the eigenvalues have the form $(\lambda_{1,2};\lambda_{3,4}) = (\pm a;\pm ib)$ regardless of the sign of β (Type 6).

B. Second case: $\rho = 1$

Here, the characteristic equation has a double root:

$$\lambda^2 = \frac{2}{\beta}[2-\alpha], \tag{25}$$

and there are two subcases:

(1) If $\beta < 0$, the eigenvalues can be written as $(\lambda_{1,2};\lambda_{3,4}) = (\pm ia;\pm ia)$ when $\alpha < 2$ (Type 7), as $(\lambda_{1,2};\lambda_{3,4}) = (0;0)$ when $\alpha = 2$ (Type 2), and as $(\lambda_{1,2};\lambda_{3,4}) = (\pm a;\pm a)$ when $\alpha > 2$ (Type 8).

(2) If $\beta > 0$, the eigenvalues are $(\lambda_{1,2};\lambda_{3,4}) = (\pm ia;\pm ia)$ when $\alpha > 2$ (Type 7), as $(\lambda_{1,2};\lambda_{3,4}) = (0;0)$ when $\alpha = 2$ (Type 2), and as $(\lambda_{1,2};\lambda_{3,4}) = (\pm a;\pm a)$ when $\alpha < 2$ (Type 8).

C. Third case: $\rho < 1$

This case corresponds to the situation where the eigenvalues are complex:

$$\lambda^2 = \frac{2}{|\beta|}[2\rho - \alpha \pm i\sqrt{1-\rho^2}]. \tag{26}$$

This kind of eigenvalues will be referred to as of Type 9, and they have the explicit form $(\lambda_{1,2};\lambda_{3,4}) = (a \pm ib; c \pm id)$ regardless of the sign of β.

V. BIFURCATION MAPS

The stability analysis developed in Sec. IV enables us to obtain bifurcation maps, which are presented in Figs. 4 and 5.

It is important to note that, in our case, the system has a $\theta \to -\theta$ symmetry: as a consequence, the spatial bifurcations that are arising in the system are necessarily *reversible*. Such reversible bifurcations have been studied in detail in the fourth chapter of Ref. [25], where a normal form characterization is provided as well. This reversibility is essential because it facilitates the study of the bifurcations. Another consequence of this symmetry is that the eigenvalue spectrum is symmetrical relatively to the imaginary axis, which in our system comes along with a symmetry relatively to the real axis. This is

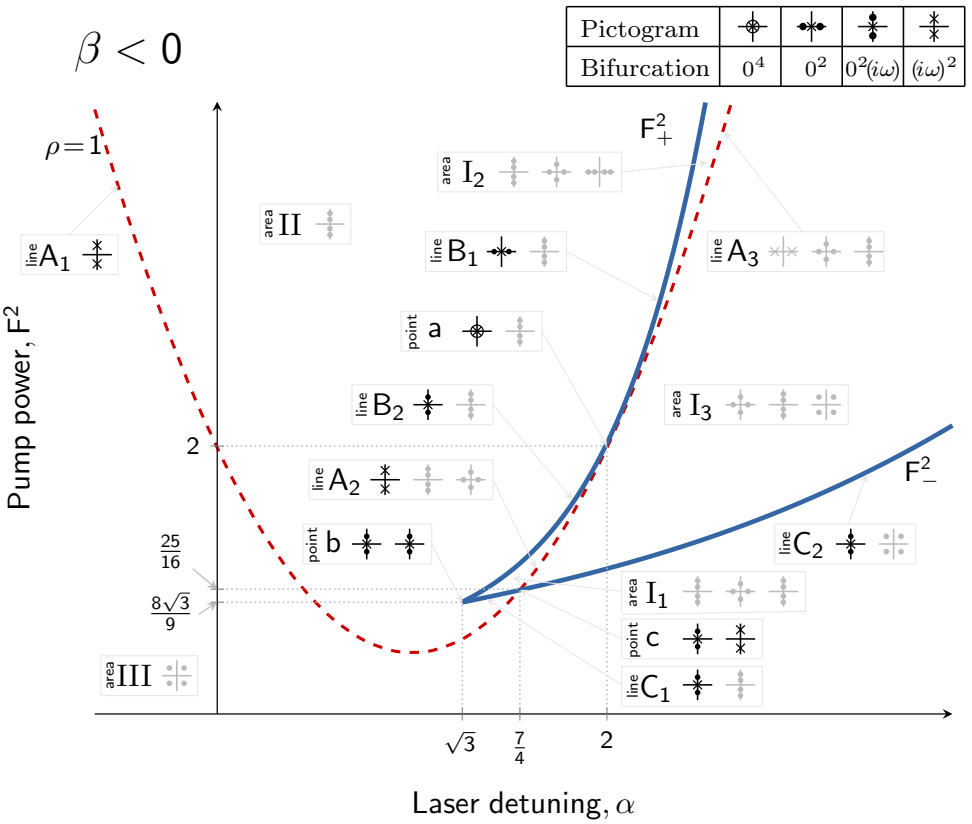

FIG. 4. (Color online) Eigenvalue bifurcation diagram (not to scale) for the case of anomalous dispersion ($\beta < 0$). The areas are labeled using Roman numerals (I, II, and III), and area I is subdivided into three subareas (I_1, I_2, and I_3). The lines are labeled using capital letters, with line A standing for the limit $\rho = 1$ (dashed line in the figure), B standing for $F_+^2(\alpha)$, and C standing for $F_-^2(\alpha)$. These lines can also be subdivided as A_1, A_2, etc. The points are labeled using lower-case letters (a and b). It is important to remember that the system has three equilibria in area I (between the two thick lines $F_\pm^2$) and has only one equilibrium in areas II and III. Therefore, there is a set of three quadruplets of spatial eigenvalues in area I, two quadruplets at the boundaries $F_\pm^2$, and one quadruplet outside. The eigenvalue pictograms are in black when they induce a bifurcation, and in gray when they do not.

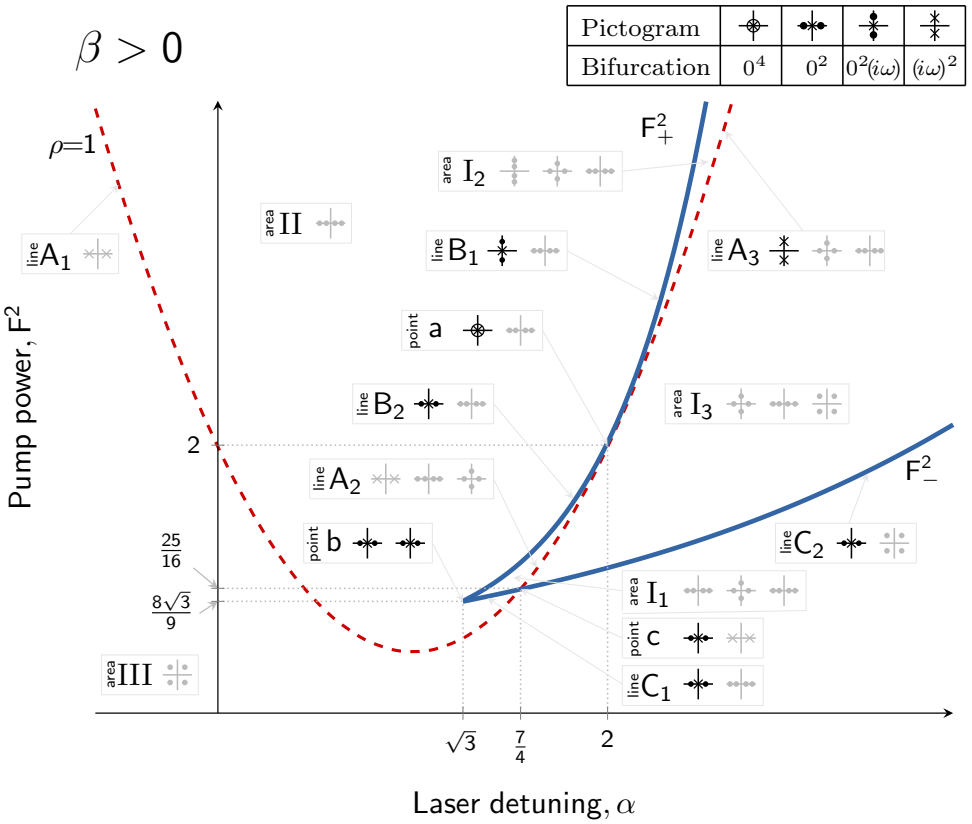

FIG. 5. (Color online) Eigenvalue bifurcation diagram (not to scale) for the case of normal dispersion ($\beta > 0$). The areas are labeled using Roman numerals (I, II, and III). The lines are labeled using capital letters, and line A stands for the limit $\rho = 1$ (dashed line in the figure), B stands for $F_+^2(\alpha)$, and C stands for $F_-^2(\alpha)$. The points are labeled using lower-case letters (a and b). Both areas and lines can be divided into subdomains (I_1, I_2, A_1, B_1, etc.) The system has three equilibria (three quadruplets of eigenvalues) in area I, one equilibrium outside (one quadruplet), and two at the boundaries (two quadruplets). Black eigenvalue pictograms denote a bifurcation according to Table I, while gray pictograms do not.

why these eigenvalues are structurally similar to those of an Hamiltonian system.

We list here the four reversible bifurcations that can be identified in Figs. 4 and 5:

(1) 0^2 bifurcation: The 0^2 bifurcation, which is also referred to as the "*Takens-Bogdanov*" bifurcation, arises when a quadruplet of eigenvalues is of Type 4. Depending on the system under study, both periodic and localized stationary solutions can eventually be sustained in the vicinity of this bifurcation.

(2) $0^2(i\omega)$ bifurcation: This bifurcation (also known as the "*Takens-Bogdanov-Hopf*" bifurcation) corresponds to a quadruplet of Type 5. Along this bifurcation, possible stationary states are periodic and quasiperiodic solutions. However, localized solutions are typically unstable near this bifurcation.

(3) $(i\omega)^2$ bifurcation: This bifurcation is sometimes referred to as the "1 : 1 resonance" or the "*Hamiltonian-Hopf*" bifurcation. It arises when a quadruplet of eigenvalues is of Type 7. Typical solutions around this bifurcation eventually include quasiperiodic, periodic, and localized solutions.

(4) 0^4 bifurcation: This is a codimension-two bifurcation, arising when a quadruplet of eigenvalues degenerates to the origin (Type 2). For this reason it is also generally referred to as a "*quadruple-zero*" bifurcation, around which a very large variety of dynamics can a priori be observed.

It should be emphasized that, even though these same four bifurcations are present in both the anomalous- and normal-GVD cases, the eigenvalue structure is totally different: in fact, all the eigenvalues are rotated by 90°, because the eigenvalues of the normal- and anomalous-GVD regimes only differ by a multiplicative factor $i = e^{i\frac{\pi}{2}}$. This *essential* difference is what explains the intrinsically different dynamics that can be witnessed in both dispersion regimes: very limited in the normal-dispersion case, and very rich when the dispersion is anomalous, as we will see later.

It is also noteworthy that, since some eigenvalues are located on the imaginary axis in the pictograms of Types 3 and 6, they also indeed correspond to bifurcations, respectively referred to as $(i\omega_1)(i\omega_2)$ and as $(i\omega)$. However, the reversibility of our system forces these eigenvalues to stay on the imaginary axis, so that these bifurcations are not dynamically relevant in our system (nonrespect of the transversality condition). This is why they are not highlighted in Table I.

A. Bifurcation map for the case of anomalous dispersion

The line A_1 corresponds to a $(i\omega)^2$ (or Hamiltonian-Hopf) bifurcation: this bifurcation at $\rho = 1 = |\psi_{\text{th}}|^2$ has been studied in much detail in Ref. [11] by using a modal-expansion approach, and it was shown that it corresponded to the

TABLE I. Nomenclature and pictograms for the various sets of eigenvalues. A set of four eigenvalues is attached to each equilibrium, and some classified bifurcations are attached to certain configurations of eigenvalues. A dot stands for one (simple) eigenvalue, the cross corresponds to a set of two degenerate eigenvalues (double nonsemisimple eigenvalue), and a circled cross stands for a set of four degenerate eigenvalues (quadruple eigenvalue with a 4×4 Jordan bloc).

Eigenvalues and reversible spatial bifurcations in the Lugiato-Lefever model						
Type	Nomenclature	Eigenvalues $(\lambda_{1,2};\lambda_{3,4})$	Pictogram	Bifurcation	Location in Fig. 4	Location in Fig. 5
1		$(\pm a;\pm b)$				
2	Quadruple-zero	$(0;0)$		0^4	a	a
3		$(\pm ia;\pm ib)$				
4	Takens-Bogdanov	$(\pm a;0)$		0^2	B_1	B_2, b, C_1, c, C_2
5	Takens-Bogdanov-Hopf	$(0;\pm ib)$		$0^2(i\omega)$	B_2, b, C_1, c, C_2	B_1
6		$(\pm a;\pm ib)$				
7	Hamiltonian-Hopf	$(\pm ia;\pm ia)$		$(i\omega)^2$	A_1, A_2	A_3
8		$(\pm a;\pm a)$				
9		$(a \pm ib;c \pm id)$				

generation of the so-called primary comb. Further analysis shows that this bifurcation corresponds in fact to modulational instability and leads to azimuthal Turing patterns [17]. From a more general perspective, it appears that, in the anomalous-GVD regime, there is always a bifurcation which separates the low-power area from the high-power area in the map, and which leads to Kerr-comb generation. As a consequence, for sufficiently high pump power, Kerr combs can always be generated in the anomalous-GVD regime for any value α of cavity detuning. The variety of solutions that can be obtained depending on the parameters and on the initial conditions is analyzed in detail in Sec. VI. This case of anomalous dispersion has also been investigated in detail in Ref. [26].

B. Bifurcation map for case of normal dispersion

At the opposite of the case of anomalous GVD, the boundary line $\rho = |\psi|^2 = 1$ *does not* correspond to a bifurcation when $\alpha < 2$. In particular, for $\alpha < \sqrt{3}$, we showed earlier that there is only one equilibrium, which is necessary stable. Hence, the bifurcation analysis indicates that increasing the pump power in that case does not lead to any modification since areas I and III do not differ structurally: this is why Kerr-comb generation is impossible for $\alpha < \sqrt{3}$ in the regime of normal dispersion. It has been thought for long time that Kerr-comb generation was absolutely impossible in the regime of normal dispersion. Numerical evidence of normal-GVD Kerr combs has in fact been obtained only very recently by using a modal-expansion model [18], and their experimental observation is fairly recent as well [9,17,27]. However, this bifurcation analysis indicates that nontrivial solutions might exist around the bifurcation lines that we have identified. We will show in Sec. VII that both extended (Turing patterns) and localized (dark solitons) dissipative structures can arise in the system, thereby leading to complex patterns in both the time and spectral domains.

VI. KERR-COMB GENERATION IN ANOMALOUS-DISPERSION REGIME

A. Turing patterns (primary combs) via modulational instability

Pattern formation in systems dynamically described by partial differential equations was investigated for the first time by Alan Turing in his seminal work of morphogenesis [28].

In our system, the so-called *Turing patterns* originate from the $(i\omega)^2$ (or Hamiltonian-Hopf) bifurcation arising at $\rho = 1$ for $\alpha < 2$ (lines A_1 and A_2 in Fig. 4).

In this section, we will mainly focus for the sake of simplification on the case $\alpha < \sqrt{3}$ where this bifurcation is the only one that can occur in the system (portion of line A_1). The emergence of Turing patterns was studied in Ref. [11] with a modal-expansion approach (where they induced the so-called *primary combs*) and compared to experimental measurements in Ref. [17,29]. In the general case of pattern formation in LLE equations, an abundant literature is indeed available, mostly in a configuration where the Laplacian term stands for diffraction instead of dispersion. Interesting references include, for example, Refs. [30,31] (and references therein), as well as Refs. [32–35] whose focus was the particular case of spatial cavity solitons.

In our case, it can be shown that Turing patterns emerge following two different scenarios, either following a supercritical bifurcation (soft excitation), or a subcritical bifurcation (hard excitation), which are analyzed here.

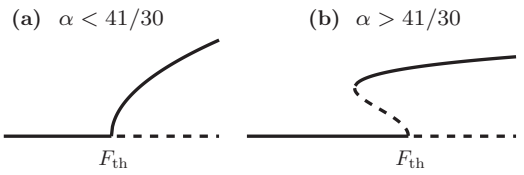

FIG. 6. Diagram showing the difference between supercritical ($\alpha < 41/30$) and subcritical ($\alpha > 41/30$) pitchfork bifurcation toward Turing patterns. The continuous line denotes a stable amplitude while the dashed line stands for an unstable steady state. (a) In the supercritical case, no Kerr comb is possible below the threshold pump power $F_{\rm th}^2$. Above this threshold, the side modes of the Kerr comb can continuously grow from infinitesimally small to significantly large as the pump is increased. The stable equilibrium and the Turing pattern are never simultaneously stable. This excitation mode is sometimes referred to as *soft*. (b) In the subcritical case, a Kerr comb is possible in a small interval *below* the threshold pump power $F_{\rm th}^2$. Moreover, in the small interval below $F_{\rm th}^2$ where the comb can be excited, a stable Turing pattern does coexist with the equilibrium solution (bistability). As a consequence, the transition from the flat state to the Turing pattern is abrupt, and the side modes of the comb cannot be infinitesimally small. This excitation mode is sometimes referred to as *hard*.

1. *Supercritical and subcritical Turing patterns*

The super- or subcritical nature if the Turing patterns originating form the LLE was already foreshadowed in the original work of Lugiato and Lefever [16]. It was later studied extensively by several research groups investigating dissipative structures in nonlinear optical cavities, and two recent noteworthy works on this topic are Refs. [36,37]. The essential difference between a super- and a subcritical pitchfork in our context is explained in Fig. 6, and it depends on how the comb emerges around the threshold pump power

$$F_{\rm th}^2 = 1 + (1-\alpha)^2, \tag{27}$$

which is obtained from Eq. (11) by setting $\rho = |\psi_{\rm th}|^2 = 1$. It can be mathematically shown that, as the critical value $\alpha_{\rm cr} = 41/30$ is crossed, the growth of the Turing rolls undergoes a structural change which is mathematically explained by the paradigm of super- and subcritical pitchfork bifurcations [16,36,37]. The numerical simulation of the LLE permits us to plot bifurcation diagrams such as in Fig. 7, where the difference between these two regimes can made evident in terms of the absence or presence of hysteresis.

On the one hand, a supercritical bifurcation in Turing patterns occurs when $\alpha < 41/30$. In this case, the unique equilibrium $\psi_{\rm e}$ is stable when below the threshold pump power $F < F_{\rm th}$ and unstable when $F > F_{\rm th}$, leading to the emergence of the Turing pattern (primary Kerr comb in the spectral domain). Above the pump threshold $F_{\rm th}$, the side modes of the Kerr comb can continuously grow from infinitesimally small to significantly large as the pump is increased. However, the homogeneous equilibrium $\psi_{\rm e}$ and the Turing pattern are never simultaneously stable. The temporal formation of these supercritical patterns is displayed in Fig. 8. It is interesting to note that the rolls are smooth and yield a Kerr comb characterized by isolated spectral lines with multiple FSR separation, the multiplicity being equal to the number of rolls.

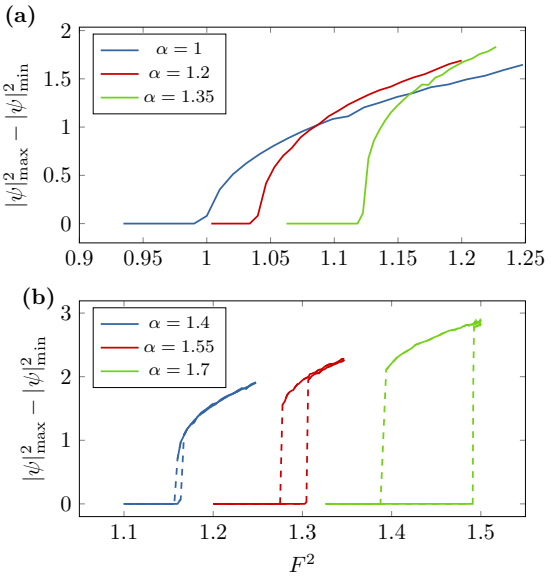

FIG. 7. (Color online) Numerical simulations showing the supercritical and subcritical nature of the Turing patterns as the detuning parameter α is varied across the critical value $\alpha_{\rm cr} = 41/30$. The other parameters are $\beta = -0.04$ and $\rho = 1.2$. (a) Growth of the pattern for the supercritical case, where $\alpha < \alpha_{\rm cr}$. It can be seen that after a critical value given by $F_{\rm th}^2 = 1 + (1-\alpha)^2$, the amplitude of the pattern grows smoothly. (b) Growth of the pattern in the subcritical case, with $\alpha > \alpha_{\rm cr}$. Here, the hysteresis area can clearly be identified when α is first smoothly swept upward, and then downward. Note that the hysteresis area increases with the detuning $\alpha - \alpha_{\rm cr}$.

On the other hand, a subcritical bifurcation to Turing patterns arises when $\alpha > 41/30$. Here, as for the supercritical case, the equilibrium $\psi_{\rm e}$ is stable for $F < F_{\rm th}$ and unstable above. However, Kerr comb is possible in a small range *below* the threshold pump power $F_{\rm th}^2$. Hence, in the small

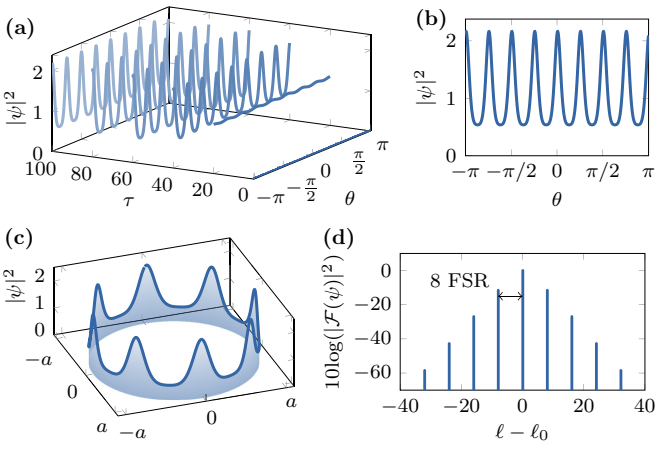

FIG. 8. (Color online) Supercritical Turing patterns (so-called *soft* excitation) generated from a small amplitude noise. The parameters are $\alpha = 1$, $\beta = -0.04$, and $\rho = 1.2$ [the pumping power F^2 can be directly calculated by using Eq. (11)]. (a) Transient dynamics. (b) Final pattern in the azimuthal direction. (c) Three-dimensional representation. (d) Corresponding Kerr comb.

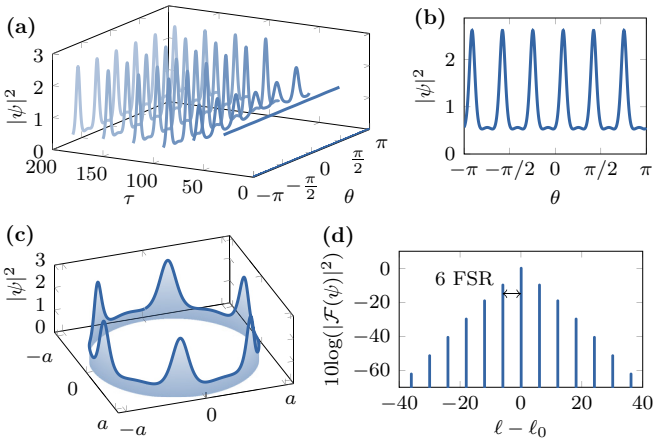

FIG. 9. (Color online) Subcritical Turing patterns (so-called *hard* excitation). The parameters are $\alpha = 1.5$, $\beta = -0.04$, and $\rho = 1.2$ [the pumping power F^2 can be directly calculated by using Eq. (11)]. (a) Transient dynamics. (b) Final pattern in the azimuthal direction. (c) Three-dimensional representation. (d) Corresponding Kerr comb.

interval below F_{th}^2 where the comb can be excited, a stable Turing pattern does coexist with the equilibrium solution. This situation creates a bistability and also induces hysteresis, as the dynamical state of the system will not be the same if the pump is adiabatically increased comparatively to when it is decreased. The consequence of this bistability is that the transition from the equilibrium to the Turing pattern is abrupt, and the side modes of the Kerr comb cannot be infinitesimally small as was the case for the supercritical case. Figure 9 shows the formation of these subcritical patterns. At the opposite of the supercritical rolls, small pedestals can be observed in this case, and the rolls also appear to be sharper.

In the context of Kerr-comb generation, the super- and subcritical bifurcation have sometimes been referred to as *soft* and *hard* excitation modes, respectively [38]. It is also noteworthy that the Turing patterns beyond $\alpha = \sqrt{3}$ are still subcritical; however, the eigenvalue structure becomes more complex because this area in the parameter space α-F^2 can encompass multiple equilibria and the four types of bifurcations listed in Sec. V. This is the area where bright cavity solitons and related structures can emerge. We will study these complex subcritical patterns in the next sections.

2. *Number of rolls in Turing patterns*

The number of rolls in the Turing pattern arising from the $(i\omega)^2$ bifurcation at $\rho = 1$ necessarily requires accounting for the boundary conditions. The reason is that, in this case, the patterns fill the whole θ domain and the number of rolls along the azimuthal direction has to be an integer. Hence, acknowledging for the modal structure of the patterns is here particularly relevant to understand this phenomenology.

According to the LLE, a perturbation $\delta\psi(\theta,\tau)$ of the equilibrium (flat solution) ψ_{e} obeys the linearized equation

$$\frac{\partial}{\partial\tau}[\delta\psi] = -(1+i\alpha)\delta\psi + 2i|\psi_{\text{e}}|^2\delta\psi + i\psi_{\text{e}}^2\delta\psi^* - i\frac{\beta}{2}\frac{\partial^2}{\partial\theta^2}[\delta\psi]. \tag{28}$$

Following Eq. (9), we can expand this perturbation according to the ansatz

$$\delta\psi(\theta,\tau) = \sum_l \delta\Psi_l(\tau)e^{il\theta}, \tag{29}$$

where $l \equiv \ell - \ell_0$ corresponds to the eigennumber of the WGMs with respect to the pumped mode ℓ_0. The interacting eigenmodes can therefore be synthetically labeled as $\pm1,\pm2,\ldots$; the mode $l = 0$ being the central mode. After inserting the ansatz of Eq. (29) into Eq. (28), we obtain an equation which can be used to perform a Hermitian projection in order to track the individual dynamics of the modal perturbations $\delta\Psi_l$. A projection onto a given mode l' consists of multiplying the equation by $e^{il'\theta}$ and integrating the product from $-\pi$ to π with respect to θ. The result of this projection yields two equations for the modal perturbations, which appear to be pairwise coupled according to

$$\begin{bmatrix}\delta\dot{\Psi}_l \\ \delta\dot{\Psi}^*_{-l}\end{bmatrix} = \begin{bmatrix}\mathcal{M} & \mathcal{N} \\ \mathcal{N}^* & \mathcal{M}^*\end{bmatrix}\begin{bmatrix}\delta\Psi_l \\ \delta\Psi^*_{-l}\end{bmatrix}, \tag{30}$$

where the overdot stands for the derivative with respect to the dimensionless time τ, while

$$\begin{aligned}\mathcal{M} &= -(1+i\alpha) + 2i|\psi_{\text{e}}|^2 + i\frac{\beta}{2}l^2, \\ \mathcal{N} &= i\psi_{\text{e}}^2.\end{aligned} \tag{31}$$

The eigenvalues of the matrix in Eq. (30) define whether a small signal perturbation (noise) in the modes $\pm l$ increases or decreases with time. In particular, the real part of the leading eigenvalue (the one with the largest real part) can be viewed as the a *gain* parameter, which can be explicitly written as

$$\Gamma(l) = \text{Re}\left\{-1 + \sqrt{\rho^2 - \left[\alpha - 2\rho - \frac{1}{2}\beta l^2\right]^2}\right\}, \tag{32}$$

where $\rho = |\psi_{\text{e}}|^2$.

At the threshold, we have already demonstrated that $\rho = 1$. On the other hand, a mode l is excited through MI when it experiences positive gain: the threshold gain can therefore be defined by $\Gamma = 0$. Hence, we deduce from the two preceding relations that, at threshold, the two modes $\pm l_{\text{th}}$ with

$$l_{\text{th}} = \sqrt{\frac{2}{\beta}(\alpha - 2)} \tag{33}$$

are excited through MI. This number also corresponds to the number of rolls that will be observed in the temporal domain. This analysis corresponds to the one that has been performed in Ref. [11] to explain the emergence of the so-called primary comb.

From a more general perspective, the modes l that can be directly excited by the pump are such that $\Gamma(l) > 0$. The

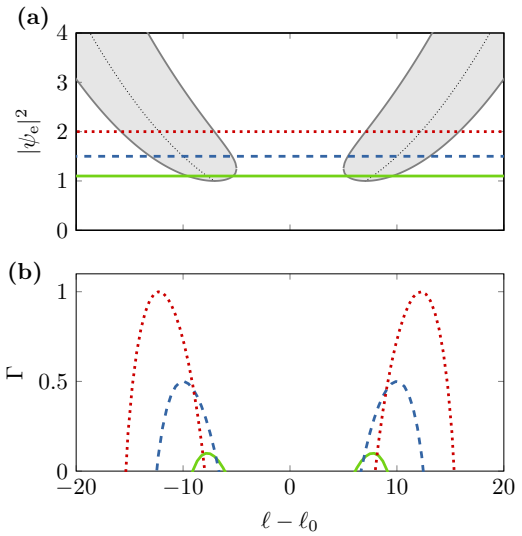

FIG. 10. (Color online) Determination of the parametric (or MI) gain in the system, with the parameters $\alpha = 1$ and $\beta = -0.04$. (a) Positive gain is experienced in the system when the figurative point is in the shaded area of the l-ρ plane, and negative gain is experienced in the white area. The densely dotted line within the shaded area indicates the location of the maximum gain. For a fixed value of ρ (that is, of the pump power F^2), the corresponding horizontal line intersects the gain area when $\rho > 1$ and thereby delimits the modes $\pm l$ which can grow through MI. (b) MI gain corresponding to the three pump levels of panel (a). Note that, as the pump power is increased, the maximum gain mode is shifted away from the pump, and the MI-gain bandwidth is both shifted outward and increased as well.

modes $\pm l_{\mathrm{mgm}}$ for which the gain is maximal are referred to as the maximum gain modes (MGMs), and they are found through the condition $\partial\Gamma/\partial l = 0$, which yields

$$l_{\mathrm{mgm}} = \sqrt{\frac{2}{\beta}(\alpha - 2\rho)}. \tag{34}$$

Figure 10 graphically displays how the MI gain leads to the emergence of a Turing pattern. When the system is pumped above threshold ($\rho > 1$), two symmetric spectral bands are created around the pump. The modes that are the most likely to arise from noise are those who have the largest gain; namely $\pm l_{\mathrm{mgm}}$. Near threshold, only two side modes (around $\pm l_{\mathrm{mgm}} \simeq \pm l_{\mathrm{th}}$) are generated and in the temporal domain: the flat background becomes unstable and leads to the emergence of the rolls, which correspond here to a sinusoidal modulation of the flat solution (from this phenomenology was coined the term "modulational instability"). However, as the pump is increased, $|l_{\mathrm{mgm}}|$ increases as well, as can be seen in Fig. 10(b). But more importantly, higher-order side modes (harmonics) are generated at eigennumbers $\pm k l_{\mathrm{mgm}}$, where k is an integer number. As a consequence, the modulation in the time domain is not sinusoidal any more, but gradually morphs into a train of sharply peaked pulses.

B. Bright cavity solitons

The existence of bright cavity solitons in nonlinear optical cavities is a well-documented topic. They arise as a balance between nonlinearity and anomalous dispersion (which defines their shape), and a balance between gain and dissipation (which defines their amplitude).

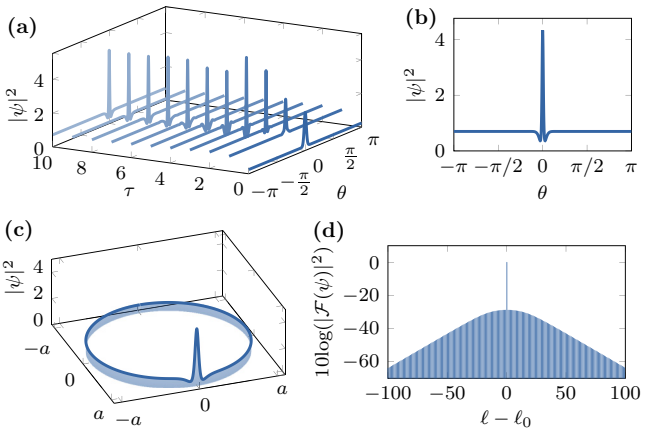

FIG. 11. (Color online) Formation of bright solitons. The parameters are $\alpha = 2$, $\beta = -0.004$, and $\rho = 0.7$, and the initial condition is a Gaussian pulse: $\psi_0 = 0.5 + \exp[-(\theta/0.1)^2]$. (a) Transient dynamics. (b) Final pattern in the azimuthal direction. (c) Three-dimensional representation. (d) Corresponding Kerr comb.

Figure 11 displays the transient dynamics toward a cavity soliton. The initial condition here is a very narrow and small pulse, which grows and converges toward a soliton characterized by a narrow pulse width and small pedestal oscillations. This soliton is subcritical because it emerged for a pump power for which the steady state is such that $\rho < 1$; hence, it does not emerge for arbitrarily small (noisy) perturbations of the intracavity background field. In fact, it can be inferred that the soliton is a pulse that has been "carved out" of a subcritical Turing pattern. This explains at the same time the subcriticality and the pedestal oscillations, which are indeed observable in subcritical Turing patterns when the detuning α is not too close to the critical value of 41/30. However, at the opposite of Turing patterns, the bright soliton is a *localized structure* in the sense that it does not feel the boundaries when they are at a distance that is significantly larger than its pulse width. Hence, the soliton of Fig. 11(c) dynamically behaves as if its background had an infinite extension. The spectrum of this soliton as presented in Fig. 11(d) has a single-FSR spacing and displays hundreds of mode-locked WGMs. Such solitons have also been observed experimentally in recent experiments [39]. It is also known that the spectral extension of this comb becomes larger as the pulses are narrower: this situation is observed when $\beta \to 0$ as discussed in Sec. VI F.

C. Bright soliton molecules

When the parameters lead to the formation of supercritical Turing patterns, the final steady state is invariably the same patterns regardless of the initial conditions (provided that there is no zero-energy mode at $\tau = 0$). For subcritical structures, the situations is indeed very different, as the final output critically depends on the initial conditions.

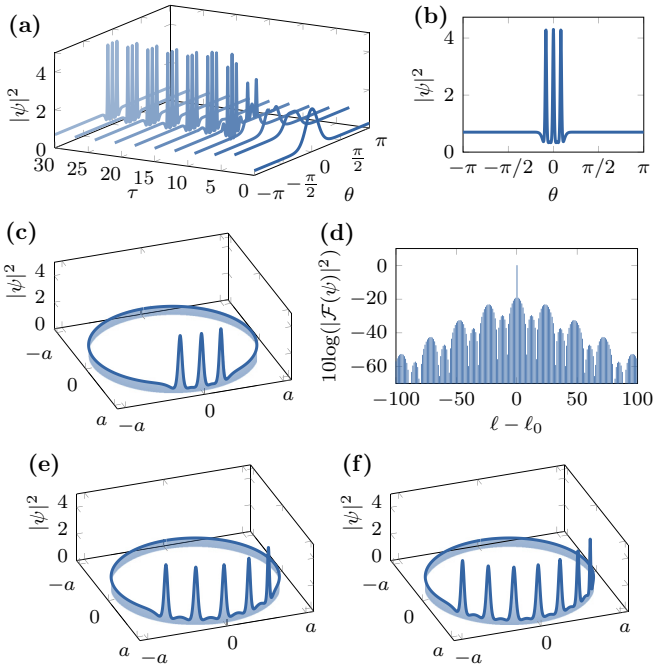

FIG. 12. (Color online) Formation of a soliton molecule. The parameters are exactly those of Fig. 11, and only the initial condition has changed (more powerful pulse): $\psi_0 = 0.5 + \exp[-(\theta/0.55)^2]$. It can be inferred that a soliton is in fact a pulse isolated from a subcritical Turing pattern, and that a soliton molecule corresponds to several of such pulses. (a) Transient dynamics. (b) Final pattern in the azimuthal direction. (c) Three-dimensional representation. (d) Corresponding Kerr comb. (e) Soliton molecule formed with five solitons obtained with $\psi_0 = 0.5 + \exp[-(\theta/0.85)^2]$. (f) Soliton molecule formed with seven solitons obtained with $\psi_0 = 0.5 + \exp[-(\theta/1.05)^2]$.

As far as solitons are concerned, the initial conditions can lead to single-peaked pulses as displayed in Fig. 11. However, more energetic initial conditions can lead to the formation of multi-peaked solutions that are here referred to as *soliton molecules*. These molecules can be considered as a limited number of pulses carved out of a subcritical Turing pattern. Figure 12 shows how the three-peaked soliton molecule is formed. This dissipative structure is subcritical and localized, exactly as the single soliton. The corresponding Kerr comb is also characterized by a single-FSR spacing, but in this case, at the opposite of what is observed in the single-peaked–soliton case, the spectrum displays a slow modulation.

For a pulse-like excitation, the number of solitons in a molecule can be controlled by the energy

$$E = \int_{-\pi}^{\pi} |\psi(\theta, \tau = 0)|^2 d\theta, \tag{35}$$

and it can be shown that the number of solitons in the molecule is governed by a snaking bifurcation [40–42]. It should be noted that these soliton molecules can also be analyzed from the viewpoint of the collective dynamics of coupled solitons [43]. Figures 12(e) and 12(f) display soliton molecules with five and seven elements, respectively, and larger numbers can be achieved as long as the molecule is blind to the finiteness of the θ domain.

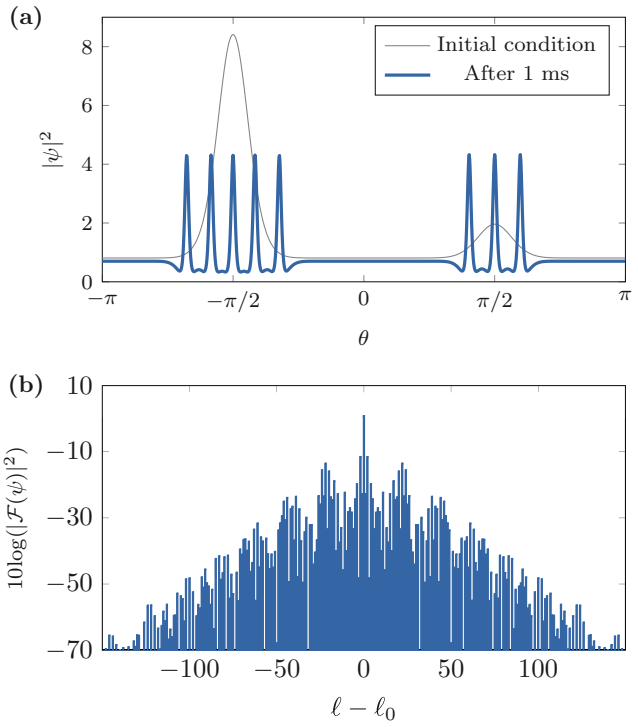

FIG. 13. (Color online) Coexistence of two soliton molecules in the resonator. The parameters are those of Fig. 11. (a) Initial conditions and final state. (b) Corresponding Kerr comb.

It is also noteworthy that different soliton molecules can coexist inside the disk. Such composite structures can be obtained, for example, by using initial conditions as displayed in Fig. 13(a). The corresponding Kerr combs look noisy, and might even wrongfully be considered as "chaotic"; however, in the time domain, the pattern is perfectly periodic and deterministic. Genuinely chaotic spectra will be studied in Sec. VI E.

Note that, if N individual and noninteracting bright solitons are exactly separated by an angle of $2\pi/N$ in the θ domain, the resulting Kerr comb will feature a multiple-FSR structure (exactly like the spectra of Turing rolls). However, even though the spectra will be similar, the dynamical states will be different because, on the one hand, we have an extended structure while, on the other hand, we have a metastable association of localized structures.

D. Breathing solitons

An interesting solution that can be obtained in the LLE is the breather soliton [44,45]. It consists of a soliton whose amplitude varies periodically in time. However, this period of the breathing is very low and is of the order of the photon lifetime. In the spectral domain, the comb corresponding to a single breathing soliton looks like that of a normal (steady) soliton, except that there are modulation side bands *inside* the modal resonance linewidths.

As displayed in Figs. 14(a) and 14(b), the breather soliton oscillates in time and approximately keeps the same pulse width. Figure 14(c) shows the oscillating behavior on a larger timescale, and it can be observed that this breather soliton

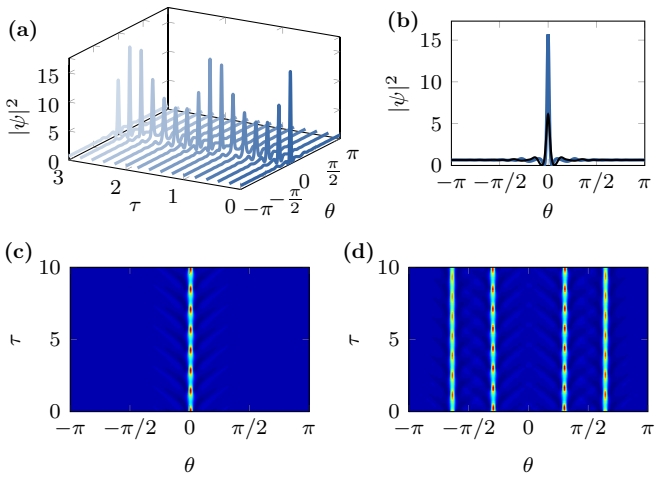

FIG. 14. (Color online) Soliton breathers. The parameters are $\alpha = 4$, $\beta = -0.04$, $\rho = 0.6$ $(F^2 = 7.54)$, and $\psi_0 = 0.5 + 0.3\exp[-(\theta/0.5)^2]$. (a) Time-domain dynamics. (b) Maximal and minimal pulse shapes. (c) Color-coded visualization of the time-domain dynamics of a soliton breather. (d) Color-coded visualization of the time-domain dynamics of a complex structure corresponding to a higher-order soliton breather. $\psi_0 = 0.5 + 2.5\exp[-(\theta/1.5)^2]$.

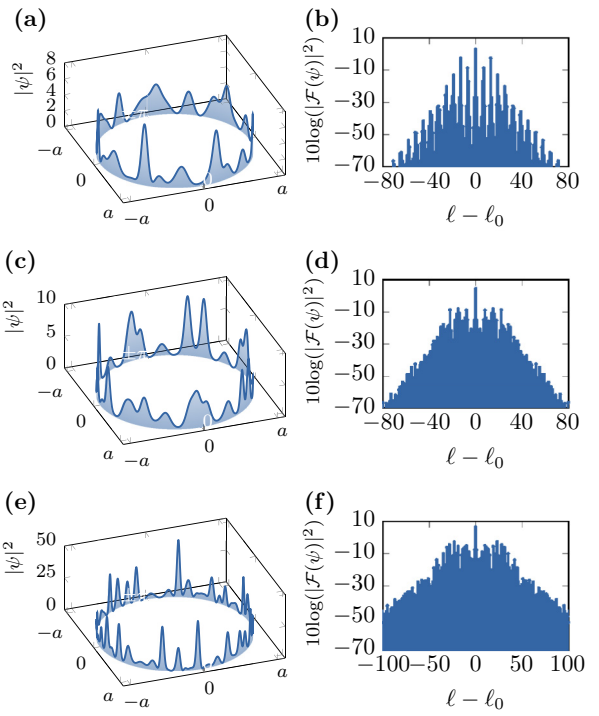

FIG. 15. (Color online) Chaos. (a) Three-dimensional (3D) snapshot of a chaotic state for $\alpha = 0$, $\beta = -0.04$, and $\rho = 1.9$. (b) Corresponding Kerr comb. (c) 3D snapshot of a chaotic state for $\alpha = 0$, $\beta = -0.04$, and $\rho = 2.5$. (d) Corresponding Kerr comb. (e) 3D snapshot of a chaotic state for $\alpha = 2$, $\beta = -0.04$, and $\rho = 3$. (f) Corresponding Kerr comb.

is a localized structure that is boundary blind. On the other hand, Fig. 14(d) presents a higher-order breather soliton with a complex structure consisting of multiple peaks that are not oscillating in synchrony. Actually, these soliton breathers can have a very wide variety of shapes and oscillation behaviors depending on the initial conditions.

E. Chaos

It is well known that chaos can potentially arise in any nonlinear system with at least three degrees of freedom. The LLE is indeed a highly nonlinear and infinite-dimensional system and, in fact, the phenomenology of interest (Kerr-comb generation) for us essentially relies on the nonlinearity.

From a practical viewpoint, almost all high-dimensional and nonlinear systems display chaos when they are strongly excited. Chaos in Kerr combs has been unambiguously spotted both theoretically and experimentally in Ref. [10], where the Lyapunov exponent was computed and shown to be positive under certain circumstances. Early studies on this topic of chaos in dissipative optical cavities include references like [46], while more recent research work in the context of Kerr-comb generation include Ref. [47].

From the preceding sections, at least two routes to chaos can be identified in this system [48].

The first route corresponds to unstable Turing patterns. Figures 15(a) and 15(b) show that, in that case, the Kerr comb is made of very strong spectral lines corresponding to the primary comb and apparent spectral lines standing in between, which are the signature to what was referred to as the secondary comb in Refs. [10,11]. Hence, in this case, the route to chaos as the pump power F^2 is increased is a sequence of bifurcations starting with the primary comb which becomes unstable and leads to the emergence of a secondary comb. Later on, higher-order combs are sequentially generated until a fully developed chaotic state is reached, as can be seen in Figs. 15(c) and 15(d).

The second route to chaos corresponds to unstable solitons. Here, as the pump power is increased, the solitons become unstable and the system enters into a "turbulent" regime characterized by the pseudorandom emergence of sharp and powerful peaks, as can be seen in Fig. 15(e). This kind of chaos gives birth in the WGM resonator to the so-called *rogue waves* [49]. It should be recalled that these waves are rare events of extreme amplitudes, and they can arise in a very wide variety of nonlinear physical systems [50]. They are particularly ubiquitous in nonlinear photonics where they have been studied extensively [51–57].

F. Influence of dispersion parameter β

The bifurcation map displayed in Fig. 16 in the α-F plane disregards the effect of the magnitude of the dispersion. Indeed, the effect induced by the value of $|\beta|$ depends on the localized or nonlocalized nature of solution under study.

More precisely, if we consider both super- and subcritical Turing patterns (nonlocalized structures), the effect of decreasing $|\beta|$ is straightforward because it increases the number of rolls according to Eq. (34) just above the pump. However, because the pump is increased beyond the bifurcation, such a decrease of $|\beta|$ also reduces the pulse width of the individual Turing rolls in the subcritical case. As far as solitons are concerned (localized structures), the effect of reducing $|\beta|$ is essentially to decrease the pulse width of the solitons (see

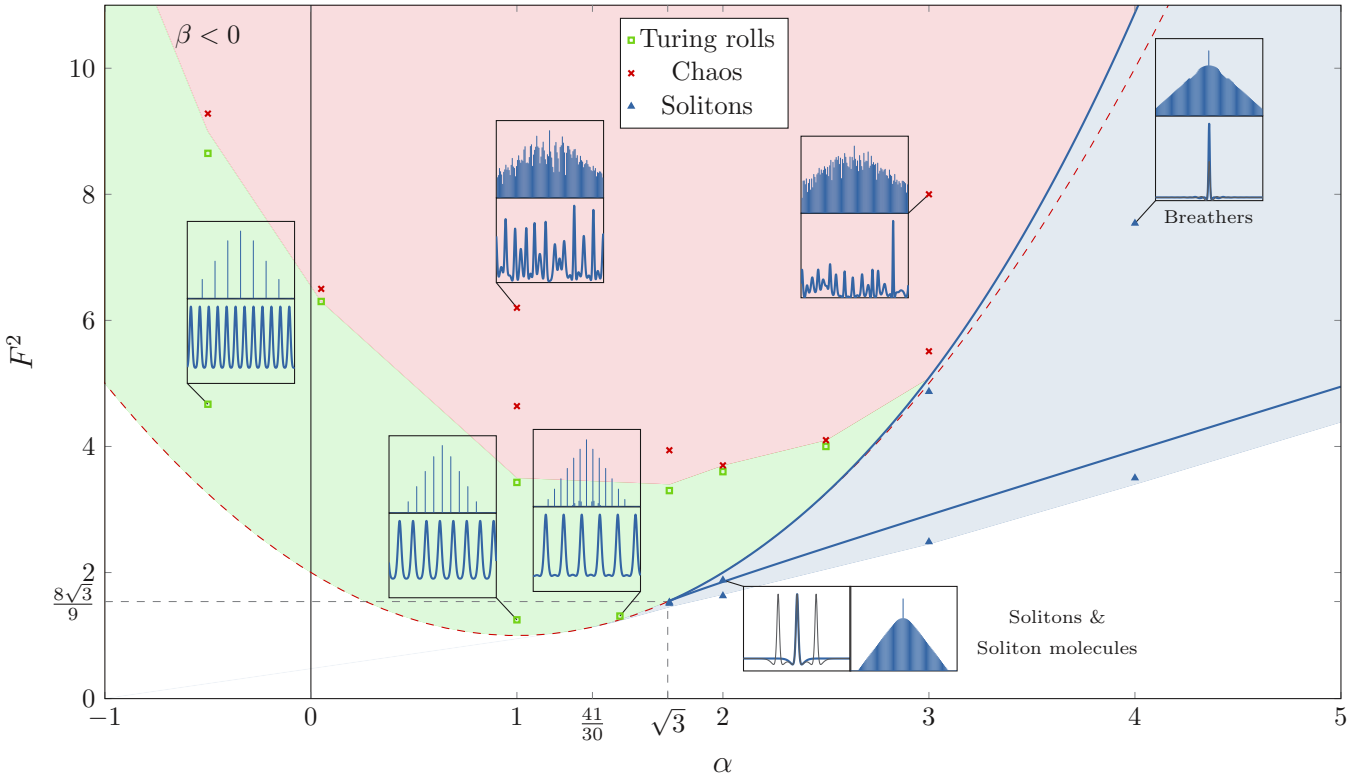

FIG. 16. (Color online) Bifurcation diagram to scale in the case of anomalous dispersion ($\beta < 0$), showing the parameters leading to various stationary solutions. Besides equilibria (flat solutions, white area), the possible solutions are Turing patterns (super- and subcritical, green area), solitons, soliton molecules, and breathers (blue area), and finally spatiotemporal chaos (red area). The connection between solitons and subcritical Turing patterns appears clearly. Note that solitons and soliton complexes are localized in the same area of this parameter space since only the initial conditions define if the final steady-state will be of one kind or the other.

Fig. 17). Subcritical Turing patterns and solitons have the same behavior in this regard, and this is a direct consequence of the fact that they are intimately connected from a topological point of view. It should be noted once again that reducing the magnitude of second-order GVD to arbitrarily small values can increase the relevance of higher-order dispersion terms in the Lugiato-Lefever model [14].

A general consequence of a decrease in $|\beta|$ is that, because the patterns have a narrower pulse width, this will generally allow for the excitation of a large number of solitons in the cavity. Accordingly, the corresponding Kerr-comb spectra will also display a higher complexity.

VII. KERR-COMB GENERATION IN NORMAL-DISPERSION REGIME

A. Modulational instability and Turing patterns

In the bifurcation map, a $(i\omega)^2$ (or Hamiltonian-Hopf) bifurcation occurs at $\rho = 1$ for $\alpha > 2$. This bifurcation therefore occurs along the line A_3 and, according to Eq. (11), the corresponding threshold pump value is $F_{\text{th}}^2 = 1 + (\alpha - 1)^2$. As extensively explained in Sec. VI A, an extended dissipative structure, sometimes referred to as a Turing pattern [28] or a primary comb [10,11], is expected to arise beyond this bifurcation line.

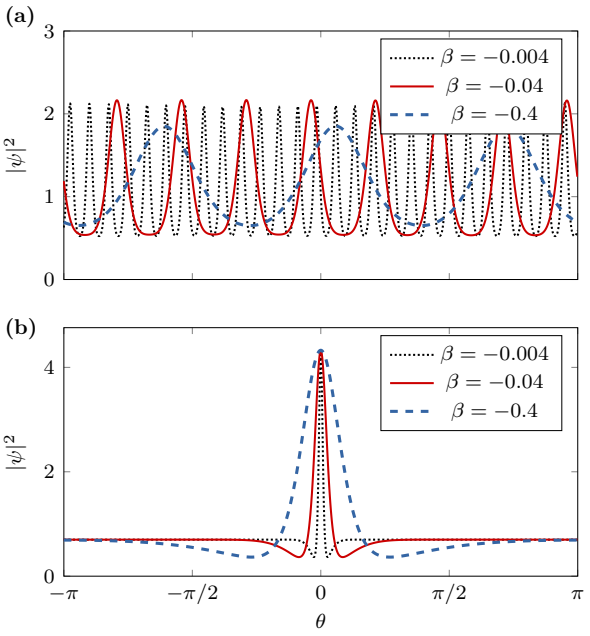

FIG. 17. (Color online) Influence of the magnitude of the dispersion parameter β. (a) Case of Turing patterns. The influence of β is essentially to change the number or rolls. (b) Case of solitons. The effect of β here is to change the pulse width.

A central characteristic of Turing patterns is that they emerge from noise. A flat solution becomes unstable, breaks down, and converges toward an azimuthal roll pattern (concept of modulational instability). In the context of Kerr frequency combs, it has long been considered that modulational instability could not arise in the normal-dispersion case. However, the trivial fixed-point analysis led in Ref. [11] using the modal-expansion model demonstrated that Turing patterns (leading to primary Kerr combs) in the normal-GVD regime can arise but are very difficult to observe. Recently, using a truncated three-mode analysis, another theoretical proof for the possibility of modulational instability was provided, as well as numerical simulations that provided evidence of normal-GVD Turing rolls in the regime of large detuning [19]. Earlier works had also investigated the mechanisms of modulational instability in dissipative ring cavities [58,59].

Here, we perform a detailed analysis that aims to provide a clear understanding of Turing-roll formation in the normal-GVD regime. In particular, we will explain here why Turing rolls are observed for large detunings only, even though the theory predicts that they arise as soon as $\alpha > 2$.

Figure 18 explicitly shows the distribution of the various equilibria ρ_1, ρ_2, and ρ_3 and critical points $\rho_\pm$ as a function of

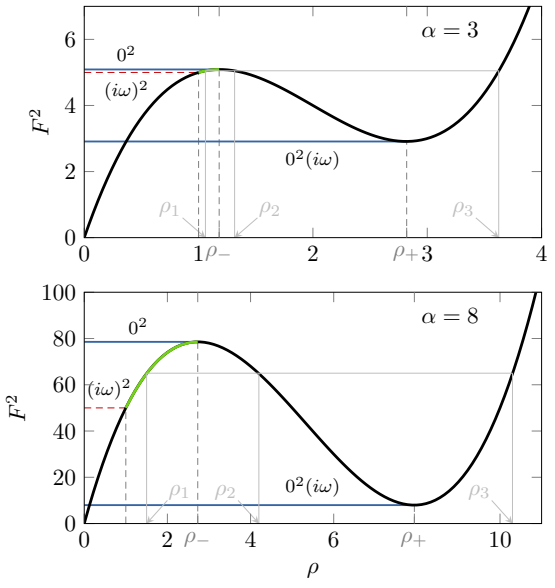

FIG. 18. (Color online) Distribution of equilibria ρ_1, ρ_2, and ρ_3 and critical points $\rho_\pm$ as a function of the detuning parameter α, and influence on the stability of Turing patterns in the normal-GVD regime. In the first case of small detuning ($\alpha = 3$), the detuning is still relatively close to the critical value $\alpha = 2$. It can be seen that the value $\rho = 1$ at threshold is still close to the critical point ρ_-. In particular, they corresponds to extremely closed value of the pump (just above $F^2_{\rm th} = 5 \simeq F^2_+$). Turing patterns in this case are very difficult to observe because once the pump value is fixed and the modulational instability is triggered, the proximity of the unstable fixed point ρ_2 will repel the system toward the stable fixed point ρ_3. In the second case of large detuning ($\alpha = 8$), the detuning is far enough from the critical value $\alpha = 2$. Here, the threshold critical value $\rho = 1$ is very far from the unstable fixed point ρ_2, and they correspond to very-well-split values of the pump $F^2_{\rm th} < F^2_+$. In this case, the modulational instability around $F^2 = 60$ (for example) will give rise to a stable Turing pattern.

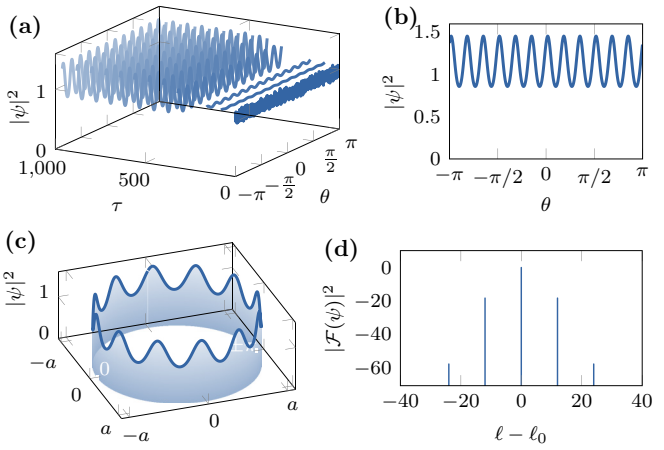

FIG. 19. (Color online) MI in the normal-GVD regime, starting with random amplitude noise in the cavity. The parameters are $\alpha = 10$, $F^2 = 68.5$, and $\beta = 0.1$.

the detuning parameter α. This repartition has a great influence on the stability of Turing patterns, as explained below.

When the detuning is still relatively close to the critical value $\alpha = 2$, the splitting between the threshold pump value $F^2_{\rm th}$ and the critical value F^2_+ is very small, while we need $F^2_{\rm th} < F^2 < F^2_+$. As a consequence, the critical power $\rho = 1$ is very close to the unstable fixed point ρ_2. Hence, the oscillation induced by the modulational instability necessarily comes very close to ρ_2 and gets repelled to the other stable fixed point; that is, to ρ_3. On the other hand, when the detuning is sufficiently large (that is, significantly larger than $\alpha = 2$), the pump value F^2 can be sufficiently far below F^+ Here, the threshold critical value $\rho = 1$ is very far from the unstable fixed point ρ_2, and they correspond to very-well-split values of the pump, and the condition $F^2_{\rm th} < F^2 < F^2_+$ can be fulfilled much more comfortably. In this case, modulational instability around $F^2 = 60$ (for example) will give rise to a stable Turing pattern (see Fig. 19).

This phenomenology explains why Turing patterns do not arise in the normal-GVD regime unless the detuning becomes large (one has to keep in mind that the pump is out of the cold-cavity resonance as soon as $|\alpha| > 1$). Turing patterns are therefore significantly more relevant and stable in the regime of anomalous dispersion.

The number of rolls in the pattern arising after the $(i\omega)^2$ (Hamiltonian-Hopf) bifurcation can also be determined analytically, following exactly the main steps of the analysis used in Sec. VI A 2. These theoretical developments show that this number is equal to $l_{\rm th} = [2(2-\alpha)/\beta]^{1/2}$ at threshold ($\rho = 1$); above threshold ($\rho > 1$), this roll number is shifted with the maximum gain mode as $l_{\rm mgm} = [2(2\rho - \alpha)/\beta]^{1/2} \geqslant l_{\rm th}$.

B. Dark cavity solitons

Dark solitons are stable localized structures characterized by a hole in a finite background (see review article [60]). In our system, the formation of these solitons appears explicitly in Fig. 20 where the temporal dynamics of the intracavity field ψ is displayed. It can be seen that, depending on the initial conditions, the final steady state of the field can either be a

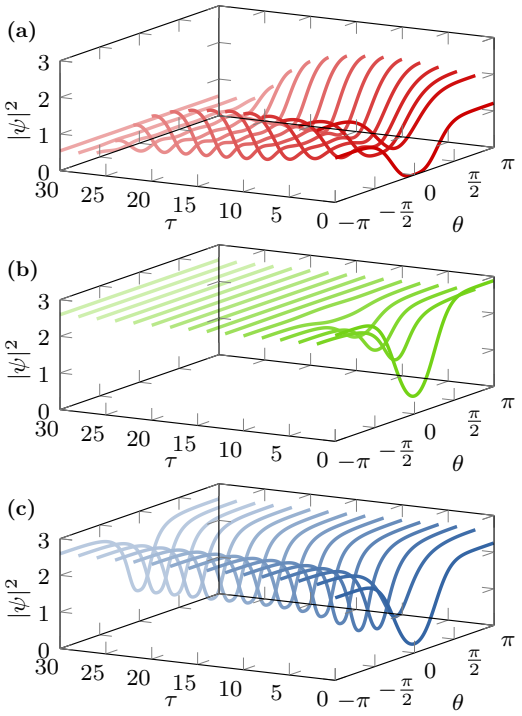

FIG. 20. (Color online) Numerical simulation of the temporal dynamics of a pulse-like perturbation in the normal-dispersion regime. The parameters are $\alpha = 2.5$, $\beta = 0.0125$, and $F^2 = 2.61$. (a) Initial condition $\psi_0 = 1.1 - \exp[-(\theta/0.9)^2]$ leading to a constant solution $\rho_1 = |\psi_{\text{down}}|^2$. (b) Initial condition $\psi_0 = 1.7 - \exp[-(\theta/0.9)^2]$ leading to a constant solution $\rho_3 = |\psi_{\text{up}}|^2$. (c) Initial condition $\psi_0 = 1.5 - \exp[-(\theta/0.9)^2]$ leading to the formation of a stable dark soliton.

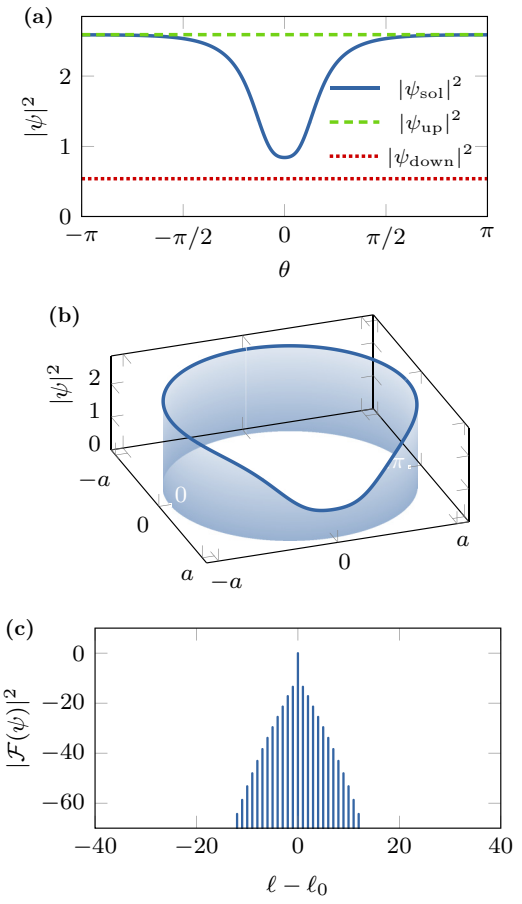

FIG. 21. (Color online) (a) Asymptotic steady state profiles of the temporal dynamics presented in Fig. 20. Note that the power profile $|\psi_{\text{sol}}|^2$ of the dark soliton lies between the "up" and "down" solutions. (b) Three-dimensional representation of a dark soliton of Fig. 20(c). (c) Corresponding Kerr comb obtained using the fast Fourier transform. The separation between the teeth corresponds to 1 FSR.

stable equilibrium [that is, a stable solution of Eq. (11)] or a dark soliton. We explained earlier that, in the three-solutions area, the intermediate solution is generally unstable whereas the extremal solutions are stable. We can see in Figs. 20(a) and 20(b) that, for the same sets of parameters, the systems may converge to the lowermost or uppermost steady-state solution, depending on the initial conditions. However, we can show that a dark soliton can appear as a stable and robust solution that is intermediate between the asymptotic levels of the two extremal steady states, as made evident in Fig. 21(a). The typical spectrum of a dark soliton is displayed in Fig. 21(c) and shows a typical triangular-like decrease of modal power away from the pump. It is noteworthy that, because there is only one pulse inside the cavity, the corresponding comb has a single-FSR spacing. These solitons have already been observed experimentally [17].

Since dark solitons are intermediate solutions between the stable equilibria in our system, they do exclusively appear in area I, where these three equilibria actually exist. However, the existence of multiple equilibria is a necessary but not sufficient condition for the emergence of stable dark solitons. As displayed in Fig. 22, our numerical simulations show that they can be observed only for a restricted range of parameters laying within a thin band inside the three-equilibrium area. A direct consequence of this observation is that no Kerr-comb generation is a priori possible in areas I and II, which are

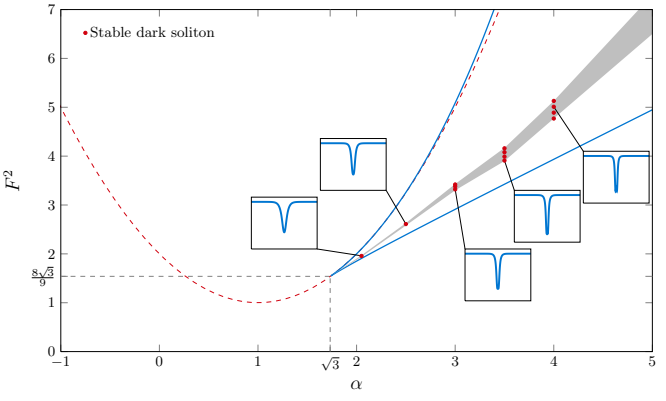

FIG. 22. (Color online) Bifurcation diagram to scale in the normal-dispersion case ($\beta > 0$), showing the parameters leading to various stationary solutions for $\alpha < 5$. Dark cavity solitons can be observed in a thin band laying within the three-equilibrium area. Out of this thin band (here approximated with straight lines), our numerical simulations have only put in evidence the convergence toward stable equilibria (flat solutions).

characterized by single equilibria. Because fairly large (out of resonance) detunings are required for the emergence of dark solitons in Fig. 22, Kerr-comb generation is very difficult to obtain experimentally in the normal-GVD regime. These combs are also likely to be only weakly stable whenever observed. Numerical simulations have also indicated that the solitons loose their stability outside the thin band displayed in Fig. 22, while one would expect the dark solitons to be stable over the whole of area I. The reason for this reduced area of stability is still unclear, but we think that it is the signature of the unstable fixed point ρ_2. Further studies are required in order to elucidate their dynamical properties in this asymptotic regime.

It is also important to note that the emergence of dark solitons depends on the initial conditions. Actually, from an experimental point of view, dark solitons will not naturally arise from noise above a certain threshold. The most likely outcome in that case would be a convergence toward the nearest flat (constant) solution, which is $\rho_1 = |\psi_{\text{down}}|^2$. Only a compact (but continuous) set of initial conditions $\psi(\theta, \tau = 0)$ can lead to the dark soliton. From this standpoint, Fig. 21 can be viewed as the result of multistability, with each stable solution ψ_{down}, ψ_{up}, and ψ_{sol} having its own basin of attraction.

The dark soliton that can be excited here is intrinsically different from the conservative dark soliton which is obtained as an exact hyperbolic tangent solution of the nonlinear Schrödinger equation with normal GVD [60]. However, in this latter case, the boundary conditions are not periodic and $\theta \in]-\infty, +\infty[$. In particular, the phase of this dark soliton is a monotonic and odd function of θ: as a consequence, this phase is null at $\theta = 0$, and the phase values at $\theta = \pm\infty$ are of opposite signs. This particular solution would then be unstable in the case of periodic boundary conditions, unless the phase jump is exactly null modulo 2π after one round trip. Figure 23 shows that the phase shift is in fact null, because the phase profile follows the pulse power profile in our case. This singular specificity of the dissipative dark soliton therefore justifies its existence in our case of periodic boundary conditions.

So far, we have analyzed the bifurcation map with regards to the two control parameters α and F. The dispersion parameter β does actually not have a direct influence on this map because we focused on localized structures and

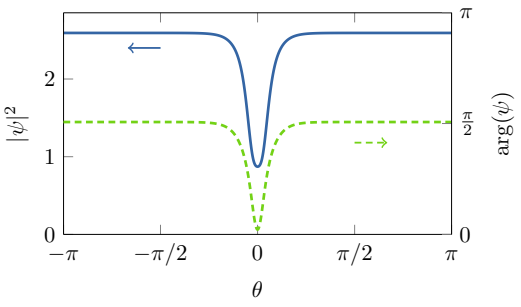

FIG. 23. (Color online) Phase of the dissipative dark soliton (same parameters as in Fig. 20). It can be seen that the phase profile is an even function which follows the power profile of pulse. The phase jump from $-\pi$ to π is null, thereby permitting the existence of this dark soliton.

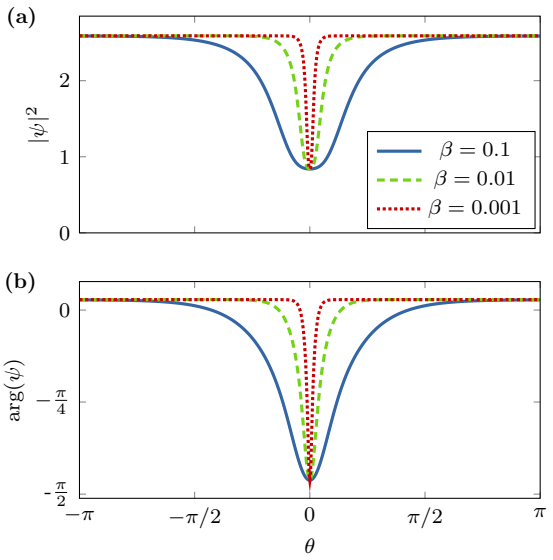

FIG. 24. (Color online) Evidence of the effect of β, showing how the soliton pulses become narrower as $\beta \to 0$. The detuning and pump parameters $\alpha = 2.5$ and $F^2 = 2.61$ are fixed, while the dispersion parameter is logarithmically varied as $\beta = 0.00125$, $\beta = 0.0125$ (same as in Fig. 20), and $\beta = 0.125$.

disregarded the boundaries. However, β has a direct influence on the temporal profile of the pulses, and particularly on their widths. Figure 24 shows that, as the dispersion decreases, the pulse width decreases as well, and the spectral spread increases accordingly. It should be noted that, from a physical standpoint, higher-order dispersion has to be included into the Lugiato-Lefever model when second-order dispersion vanishes [14]. Since the pulses become narrower as $\beta \to 0$, it also becomes easier to excite a large number of solitons in the cavity, following the scenario explained in Sec. VII C, and the corresponding Kerr-comb spectra will also display increasingly complicated patterns.

Figure 25 displays a global overview of the dynamical behavior that can be observed in our system. It can be seen that, when the detuning α is increased, the dark solitons become distorted, and further increase leads to a breathing behavior. For higher pump powers, Turing patterns can be excited just above the Hamilonian-Hopf bifurcation an $\rho = 1$, provided that the detuning is large enough, as explained in Fig. 18 and Sec. VII A.

C. Coexistence of dark cavity solitons

The dark solitons that were investigated in the last section are localized dissipative structures: they do not see the boundary conditions and, actually, they could be observed as well if the background support were extended to infinity. Hence, multiple dark cavity solitons can coexist in the cavity as long as they are far away from each other and cannot "feel" each other's influence (they are not bounded).

This situation is presented, for example, in Fig. 26 where two solitons are excited inside the cavity with a double-pulse initial condition. In this case, the solitons have been evenly spaced (separation of π) and, as a consequence, the corresponding Kerr comb has a two FSR separation.

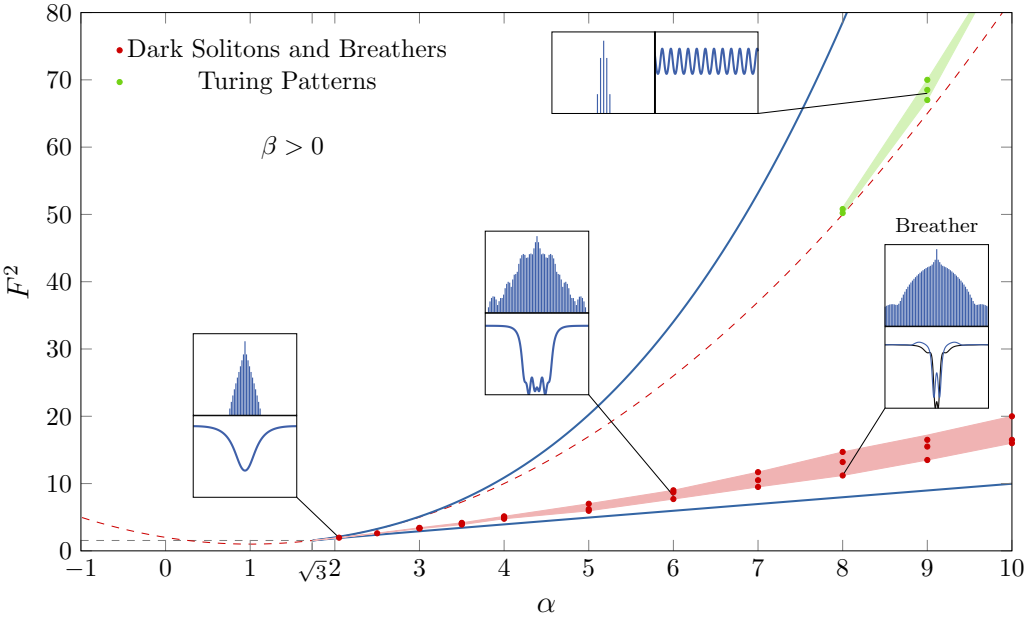

FIG. 25. (Color online) Bifurcation diagram at scale in the normal-dispersion case ($\beta > 0$), showing the parameters leading to both localized and extended dissipative structures. Dark cavity solitons can still be observed in a thin red band laying within the three-equilibrium area. As the detuning is increased, the pulse profile gets distorted, and later on gives rise to breathers. Turing patterns with multi-FSR spacing arise via modulational instability above the line $\rho = 1$ when the detuning is sufficiently large.

A more complex case is presented in Fig. 27, where three unevenly spaced solitons are excited inside the cavity. The corresponding spectra has single-FSR separation but displays a very complex pattern. Indeed, if the pulses were equidistant, the Kerr comb would have displayed a three-FSR separation. These multiple-FSR combs will generally appear whenever we have N identical dark solitons separated by a $2\pi/N$ angle. However, this symmetry is fragile and will be broken by nonidentical and/or nonequidistant pulses, yielding nontrivial Kerr-comb spectra. Of course, these spectra should not be referred to as "chaotic" or "noisy," since the corresponding time-domain solutions are perfectly periodic and deterministic.

It is worth noting that, in the multiple-pulse regime, each pulse is identical to the solitary pulse presented in Fig. 21(b). Reaching the single- or multiple-soliton states only depends

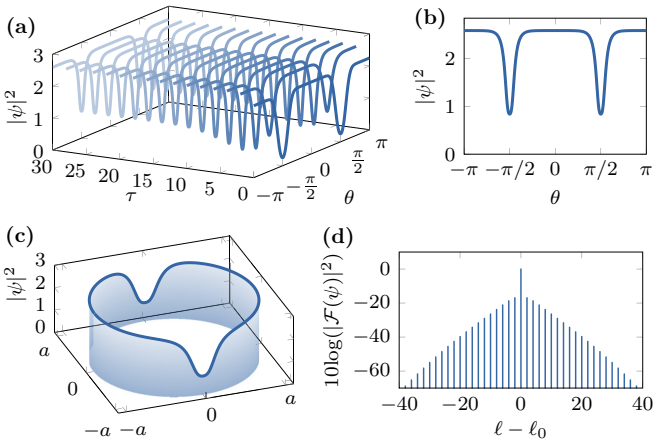

FIG. 26. (Color online) (a) Temporal dynamics leading to a the formation of two solitons in the cavity. The pulses are evenly spaced in this case (separated by π and dips at $\pm\pi/2$). The parameters are those of Fig. 20, which are $\alpha = 2.5$, $\beta = 0.0125$, and $F^2 = 2.61$, so that each pulse is identical to the isolated pulse presented in Figs. 20(c) and 21(b) at $\tau = +\infty$. (b) Three-dimensional representation. (c) Corresponding Kerr comb. Note that the separation between the teeth corresponds to two FSRs.

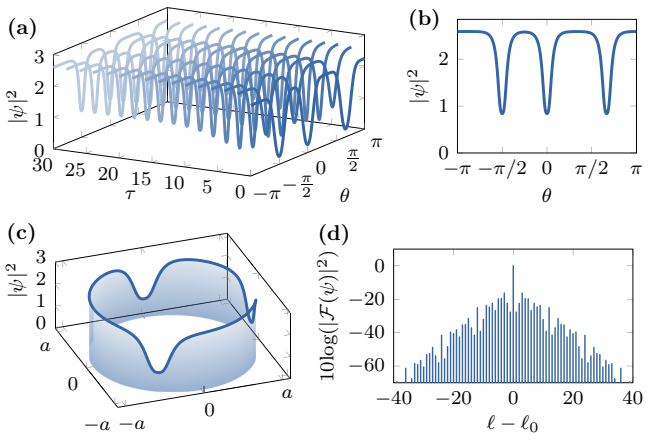

FIG. 27. (Color online) Coexistence of three solitons in the cavity with $\alpha = 2.5$, $\beta = 0.0125$, and $F^2 = 2.61$ (same as in Fig. 20). (a) Temporal dynamics leading to a the formation of three solitons in the cavity. Note that the solitons are not evenly spaced (dips at $-2\pi/3$, 0, and $\pi/2$). (b) Three-dimensional representation. (c) Corresponding Kerr comb. The separation between the teeth is equal to single FSR, but because of the nonequidistance of the pulses (which are, however, identical in shape), the comb looks "irregular." A three-FSR comb would have been obtained if the pulses (which are identical) were also equidistant and separated by $2\pi/3$.

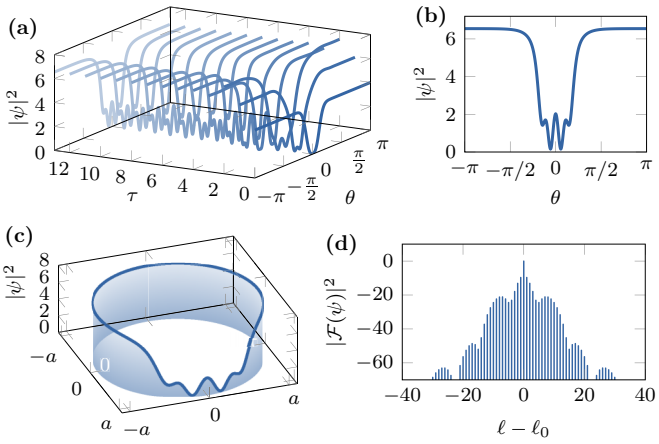

FIG. 28. (Color online) Complex dark soliton. The parameters are $\alpha = 6$, $F^2 = 8.5$ and the initial condition is $\psi_0 = 2 - 1.8\exp[-(\theta/0.35)^2]$.

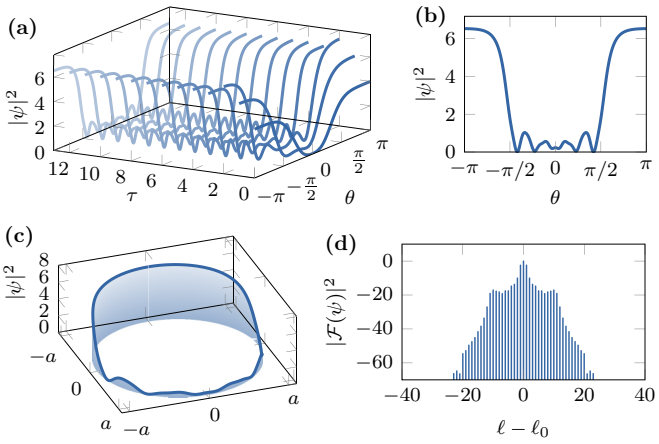

FIG. 29. (Color online) Complex dark soliton. The parameters are the same as in Fig. 28, but the initial conditions have been changed to $\psi_0 = 2 - 1.8\exp[-(\theta)^2]$.

on the initial condition. Therefore, these nonbounded multiple-soliton states emerge in the shaded area of the parameter space area in Fig. 22, exactly as single-pulse localized structures.

D. Nonsmooth and breather dark cavity solitons

Depending on the initial conditions, nontrivial dark solitons can emerge as well.

Figures 28 and 29 display, for example, some typical temporal profiles of dark solitons whose asymptotic profile is stationary but not smooth. It can be noted that the asymptotic value and the width of the nonsmooth soliton strongly depends on the initial conditions. It is still to be investigated if this complex dark soliton is actually a similariton [61] or a related dissipative structure.

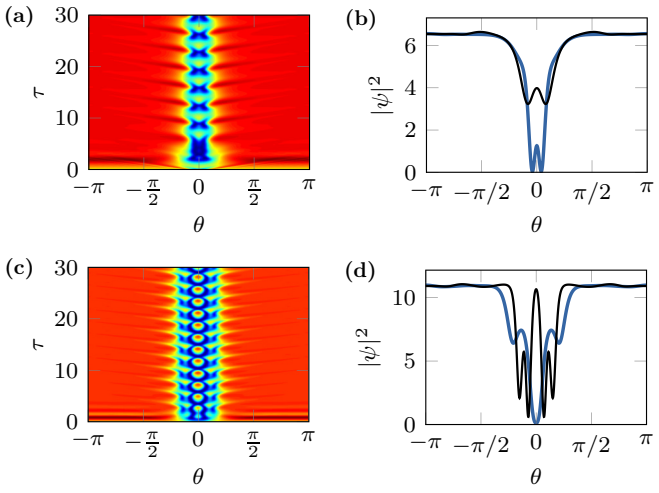

FIG. 30. (Color online) Dark soliton breathers. (a) Breather generated with the same parameters as in Figs. 28 and 29, with initial condition: $\psi_0 = 2 - 1.8\exp[-(\theta/0.1)^2]$. (b) Extremal profiles of the breather of panel (a). (c) Breather with $\alpha = 10$, $F^2 = 20$, and initial condition $\psi_0 = 2.6 - 1.4\exp(\pi\theta/10)$. (d), (b) Extremal profiles of the breather of panel (c).

These complex solitons can become breathers when the laser pump is further detuned toward larger positive values of α. Examples of such breathers are displayed in Fig. 30.

VIII. CONCLUSION

In this article, we investigated the bifurcation structure of the Lugiato-Lefever equation which is used to model Kerr-comb generation using WGM resonators.

In the regime of anomalous dispersion, our analysis has put into evidence a plethora of possible steady states. Turing patterns arise in the system through a super- or subcritical-nature pitchfork bifurcation, which is here intrinsically associated with a $(i\omega)^2$ spatial bifurcation. The threshold for these patterns can be analytically determined, as well as the number of rolls. We were also able to determine analytically the parametric gain allowing modulational instability. We also showed how the super- or subcritical nature of the patterns affects their temporal dynamics and the way they can be excited. Our investigations also enabled us to analyze the formation of solitons. We showed that more complex structures, referred to as soliton molecules, can be generated as well in the system and can eventually coexist along the azimuthal direction of the resonator. Breather solitons were analyzed as well, and we also investigated the emergence of chaos in the system. The complexity of the related Kerr combs was also studied and discussed.

In the regime of normal dispersion, the nontrivial solutions we investigated are Turing patterns and dark cavity solitons. In this regard, the single-equilibrium area (which encompasses the in-resonance pumping regime) appeared to be unsuitable for Kerr-comb generation. This analysis showed that Turing patterns can hardly arise straightforwardly from noise in the normal-GVD regime, because the Turing patterns are stable only for large frequency detunings. On the other hand, dark solitons are preferably excited for suitable initial conditions only, so that they are not easy to excite either. However, we showed that, whenever they can be excited, dark solitons can coexist in the cavity as long as they do not interact with each other. We also showed that the dark solitons can display a breathing time-domain dynamics.

Future work will be devoted to the investigation of the effect of higher-order nonlinearity and dispersion [14,62–65], and to the tailoring of the spectral characteristics of the combs for various technological applications [66–70]. A particularly promising perspective would be to use the WGM resonator in optoelectronics applications or microwave photonics systems where its storage capacities would be an asset, along with the frequency-conversion capability provided by the Kerr nonlinearity [71–75].

ACKNOWLEDGMENTS

The authors would like to thank Mariana Haragus for very insightful comments and suggestions. The authors acknowledge financial support from the European Research Council through the project NextPhase (ERC StG 278616), and from the LabEx ACTION (project AMELL). The authors would also like to acknowledge the support of the *Mésocentre de Calcul de Franche-Comté*.

[1] T. J. Kippenberg, R. Holzwarth, and S. A. Diddams, Science **332**, 555 (2011).
[2] F. Ferdous, H. Miao, D. E. Leaird, K. Srinivasan, J. Wang, L. Chen, L. T. Varghese, and A. M. Weiner, Nat. Photonics **5**, 770 (2011).
[3] A. A. Savchenkov, A. B. Matsko, W. Liang, V. S. Ilchenko, D. Seidel, and L. Maleki, Nat. Photonics **5**, 293 (2011).
[4] S. B. Papp and S. A. Diddams, Phys. Rev. A **84**, 053833 (2011).
[5] P. Del'Haye, S. B. Papp, and S. A. Diddams, Phys. Rev. Lett. **109**, 263901 (2012).
[6] T. Herr, K. Hartinger, J. Riemensberger, C. Y. Wang, E. Gavartin, R. Holzwarth, M. L. Gorodetsky, and T. J. Kippenberg, Nat. Photonics **6**, 480 (2012).
[7] C. Y. Wang, T. Herr, P. Del'Haye, A. Schliesser, J. Hofer, R. Holzwarth, T. W. Haensch, N. Picqué, and T. J. Kippenberg, Nat. Commun. **4**, 134 (2013).
[8] A. Coillet, R. Henriet, K. P. Huy, M. Jacquot, L. Furfaro, I. Balakireva, L. Larger, and Y. K. Chembo, J. Vis. Exp. **78**, e50423 (2013).
[9] A. A. Savchenkov, A. B. Matsko, D. Strekalov, M. Mohageg, V. S. Ilchenko, and L. Maleki, Phys. Rev. Lett. **93**, 243905 (2004).
[10] Y. K. Chembo, D. V. Strekalov, and N. Yu, Phys. Rev. Lett. **104**, 103902 (2010).
[11] Y. K. Chembo and N. Yu, Phys. Rev. A **82**, 033801 (2010).
[12] I. H. Agha, Y. Okawachi, and A. L. Gaeta, Opt. Express **17**, 16209 (2009).
[13] A. B. Matsko, A. A. Savchenkov, W. Liang, V. S. Ilchenko, D. Seidel, and L. Maleki, Opt. Lett. **36**, 2845 (2011).
[14] Y. K. Chembo and C. R. Menyuk, Phys. Rev. A **87**, 053852 (2013).
[15] S. Coen, H. G. Randle, T. Sylvestre, and M. Erkintalo, Opt. Lett. **38**, 37 (2013).
[16] L. A. Lugiato and R. Lefever, Phys. Rev. Lett. **58**, 2209 (1987).
[17] A. Coillet, I. Balakireva, R. Henriet, K. Saleh, L. Larger, J. M. Dudley, C. R. Menyuk, and Y. K. Chembo, IEEE Photonics J. **5**, 6100409 (2013).
[18] A. B. Matsko, A. A. Savchenkov, and L. Maleki, Opt. Lett. **37**, 43 (2012).
[19] T. Hansson, D. Modotto, and S. Wabnitz, Phys. Rev. A **88**, 023819 (2013).
[20] A. B. Matsko and V. S. Ilchenko, IEEE J. Sel. Top. Quantum Electron. **12**, 3 (2006).
[21] A. Chiasera, Y. Dumeige, P. Féron, M. Ferrari, Y. Jestin, G. Nunzi Conti, S. Pelli, S. Soria, and G. C. Righini, Laser Photonics Rev. **4**, 457 (2010).
[22] H. A. Haus, *Waves and Fields in Optoelectronics* (Prentice-Hall, Englewood Cliffs, New Jersey, 1984), Chpt. 7.
[23] A. Coillet, R. Henriet, P. Salzenstein, K. Phan-Huy, L. Larger, and Y. K. Chembo, IEEE J. Sel. Top. Quantum Electron. **19**, 6000112 (2013).
[24] T. Hansson, D. Modotto, and S. Wabnitz, Opt. Commun. **312**, 134 (2014).
[25] M. Haragus and G. Iooss, *Local Bifurcations, Center Manifolds, and Normal Forms in Infinite-Dimensional Dynamical Systems* (Springer, 2010).
[26] P. Parra-Rivas, D. Gomila, M. A. Matias, S. Coen, and L. Gelens, Phys. Rev. A **89**, 043813 (2014).
[27] P.-H. Wang, Y. Xuan, L. Fan, L. T. Varghese, J. Wang, Y. Liu, X. Xue, D. E. Leaird, M. Qi, and A. M. Weiner, Opt. Express **21**, 22441 (2013).
[28] A. M. Turing, Philos. Trans. R. Soc., B **237**, 37 (1952).
[29] A. Coillet and Y. K. Chembo, Opt. Lett. **39**, 1529 (2014).
[30] L. A. Lugiato, IEEE J. Quantum Electron. **39**, 193 (2003).
[31] *Dissipative Solitons: From Optics to Biology and Medicine*, Lect. Notes Phys., edited by N. Akhmediev and A. Ankiewicz (2008), Vol. 751.
[32] A. J. Scroggie, W. J. Firth, G. S. McDonald, M. Tlidi, R. Lefever, and L. A. Lugiato, Chaos, Solitons Fractals **4**, 1323 (1994).
[33] M. Santagiustina, P. Colet, M. San Miguel, and D. Walgraef, Phys. Rev. Lett. **79**, 3633 (1997).
[34] W. J. Firth, G. K. Harkness, A. Lord, J. M. McSloy, D. Gomila, and P. Colet, J. Opt. Soc. Am. B **19**, 747 (2002).
[35] D. Gomila, M. A. Matias, and P. Colet, Phys. Rev. Lett. **94**, 063905 (2005).
[36] T. Miyaji, I. Ohnishi, and Y. Tsutsumi, Phys. D **239**, 2066 (2010).
[37] G. Kozyreff, Phys. D **241**, 939 (2012).
[38] A. B. Matsko, A. A. Savchenkov, V. S. Ilchenko, D. Seidel, and L. Maleki, Phys. Rev. A **85**, 023830 (2012).
[39] T. Herr, V. Brasch, J. D. Jost, C. Y. Wang, N. M. Kondratiev, M. L. Gorodetsky, and T. J. Kippenberg, Nat. Photonics **8**, 145 (2014).
[40] P. D. Woods and A. R. Champneys, Phys. D **129**, 147 (1999).
[41] J. Knobloch and T. Wagenknecht, Phys. D **206**, 82 (2005).
[42] D. Gomila, A. Scroggie, and W. Firth, Phys. D **227**, 70 (2007).
[43] I. V. Barashenkov, Yu. S. Smirnov, and N. V. Alexeeva, Phys. Rev. E **57**, 2350 (1998).
[44] A. B. Matsko, A. A. Savchenkov, and L. Maleki, Opt. Lett. **37**, 4856 (2012).
[45] F. Leo, L. Gelens, P. Emplit, M. Haelterman, and S. Coen, Opt. Express **21**, 9180 (2013).
[46] M. Haelterman, S. Trillo, and S. Wabnitz, Opt. Commun. **93**, 343 (1992).

[47] A. B. Matsko, W. Liang, A. A. Savchenkov, and L. Maleki, Opt. Lett. **38**, 525 (2013).
[48] A. Coillet and Y. K. Chembo, Chaos **24**, 013113 (2014).
[49] A. Coillet, J. Dudley, G. Genty, L. Larger, and Y. K. Chembo, Phys. Rev. A **89**, 013835 (2014).
[50] *Rogue Waves—Toward a Unifying Concept*, Eur. Phys. J. Spec. Top., edited by N. Akhmediev and E. Pelinovsky (Springer-Verlag, 2010), Vol. 185.
[51] D. R. Solli, C. Ropers, P. Koonath, and B. Jalali, Nature (London) **450**, 1054 (2007).
[52] B. Kibler, J. Fatome, C. Finot, G. Millot, F. Dias, G. Genty, N. Akhmediev, and J. M. Dudley, Nat. Phys. **6**, 790 (2010).
[53] C. Bonatto, M. Feyereisen, S. Barland, M. Giudici, C. Masoller, J. R. Rios Leite, and J. R. Tredicce, Phys. Rev. Lett. **107**, 053901 (2011).
[54] A. N. Pisarchik, R. Jaimes-Reátegui, R. Sevilla-Escoboza, G. Huerta-Cuellar, and M. Taki, Phys. Rev. Lett. **107**, 274101 (2011).
[55] F. T. Arecchi, U. Bortolozzo, A. Montina, and S. Residori, Phys. Rev. Lett. **106**, 153901 (2011).
[56] C. Lecaplain, P. Grelu, J. M. Soto-Crespo, and N. Akhmediev, Phys. Rev. Lett. **108**, 233901 (2012).
[57] N. Akhmediev, J. M. Dudley, D. R. Solli, and S. K. Turitsyn, J. Opt. (Bristol, UK) **15**, 060201 (2013).
[58] M. Trillo and S. Wabnitz, Opt. Lett. **17**, 745 (1992).
[59] M. Haelterman, S. Trillo, and S. Wabnitz, Opt. Commun. **91**, 401 (1992).
[60] B. Luther-Davies and Y. S. Kivshar, Phys. Rep. **298**, 81 (1998).
[61] J. M. Dudley, C. Finot, D. J. Richardson, and G. Millot, Nat. Phys. **3**, 597 (2007).
[62] M. Tlidi, L. Bahloul, L. Cherbi, A. Hariz, and S. Coulibaly, Phys. Rev. A **88**, 035802 (2013).
[63] P. Colet, M. A. Matias, L. Gelens, and D. Gomila, Phys. Rev. E **89**, 012914 (2014).
[64] L. Gelens, M. A. Matias, D. Gomila, T. Dorissen, and P. Colet, Phys. Rev. E **89**, 012915 (2014).
[65] P. Parra-Rivas, D. Gomila, F. Leo, S. Coen, and L. Gelens, arXiv:1403.0903.
[66] Y. K. Chembo and N. Yu, Opt. Lett. **35**, 2696 (2010).
[67] I. S. Grudinin, L. Baumgartel, and N. Yu, Opt. Express **20**, 6604 (2012).
[68] I. S. Grudinin, L. Baumgartel, and N. Yu, Opt. Express **21**, 26929 (2013).
[69] M. R. E. Lamont, Y. Okawachi, and A. L. Gaeta, Opt. Lett. **38**, 3478 (2013).
[70] S. Coen and M. Erkintalo, Opt. Lett. **38**, 1790 (2013).
[71] V. S. Ilchenko and A. B. Matsko, IEEE J. Sel. Top. Quantum Electron. **12**, 15 (2006).
[72] Y. K. Chembo, A. Hmima, P.-A. Lacourt, L. Larger, and J. M. Dudley, J. Lightwave Technol. **27**, 5160 (2009).
[73] K. Volyanskiy, P. Salzenstein, H. Tavernier, M. Pogurmirskiy, Y. K. Chembo, and L. Larger, Opt. Express **18**, 22358 (2010).
[74] R. Henriet, A. Coillet, K. Saleh, L. Larger, and Y. K. Chembo, Opt. Eng. **53**, 071821 (2014).
[75] R. Martinenghi, S. Rybalko, M. Jacquot, Y. K. Chembo, and L. Larger, Phys. Rev. Lett. **108**, 244101 (2012).